

Gamma-Rays from Single Lobe Supernova Explosions

Aimee L. Hungerford

Transport Methods, Los Alamos National Laboratories,
Los Alamos, NM 87545

Chris L. Fryer¹, Gabriel Rockefeller¹

Theoretical Astrophysics, Los Alamos National Laboratories,
Los Alamos, NM 87545

ABSTRACT

Multi-dimensional simulations of the neutrino-driven mechanism behind core-collapse supernovae have long shown that the explosions from this mechanism would be asymmetric. Recently, detailed core-collapse simulations have shown that the explosion may be strongest in a single direction. We present a suite of simulations modeling these “single-lobe” supernova explosions of a $15 M_{\odot}$ red supergiant star, focusing on the effect these asymmetries have on the gamma-ray emission and the mixing in the explosion. We discuss how these asymmetries in the explosion mechanism might explain many of the observed “asymmetries” of supernovae, focusing on features of both supernova 1987A and the Cas A supernova remnant. In particular, we show that single-lobe explosions provide a promising solution to the redshifted iron lines of supernova 1987A. We also show that the extent of mixing for explosive burning products depends sensitively on the angular profile of the velocity asymmetry and can be much more extensive than previously assumed.

Subject headings: stars: supernovae—stars: neutron

1. Introduction

Observational evidence for asymmetries in core-collapse supernovae (SNe) has been mounting for more than a decade (see Wang et al. 2001 and Hungerford, Fryer & Warren 2003, hereafter HFW03, for a review). High energy observations of SN 1987A were among

¹Also at: Physics Department, University of Arizona, Tucson, AZ, 85721

the first to indicate that our assumptions of spherical symmetry were inadequate. The Comptonized hard X-ray continuum (Dotani et al. 1987; Sunyaev et al. 1987) was detected nearly 6 months earlier than spherically symmetric SN models predicted, and the MeV decay lines (Tueller et al. 1990) were much broader than what then-current theories could explain. The earlier emergence and broader line profiles both argued for the existence of a small amount of radioactive nickel mixed closer to the surface of the ejecta (see Arnett et al. 1989 for a review.) In addition, spherically symmetric models predicted blueshifted line centroids (since the receding side of the SN ejecta is at large optical depth), but the γ -ray observations showed redshifted line profiles. Although the γ -ray data uncertainties were quite high, this redshift was also observed in the infrared forbidden lines of [FeII] and [CoII], providing support for the γ -ray line centroid measurements². An early study by Grant & Dean (1993) demonstrated that models with lopsided ^{56}Ni distributions were capable of reproducing the observed γ -ray line redshifts towards SN 1987A. While their treatment of the asymmetry was at the level of a toy model, and the extent of the assumed asymmetry was rather extreme, their work demonstrated the need for a large-scale, low mode asymmetry in the ^{56}Ni distribution.

Observations at other wavelengths also support the existence of large-scale asymmetry in the explosion mechanism. Significant optical polarization has been observed toward several core-collapse supernovae over the past decade (Leonard & Filippenko 2001; Wang et al. 2001), confirming that global asymmetries are a property of the entire class of core-collapse supernovae. Most interesting is that these observations show increasing polarization with time, suggesting that it is the explosion mechanism driving these supernovae which imprints the asymmetry (Höfllich 1991). Models of the nucleosynthetic yields from SN 1987A and Cassiopeia A supernova remnant (SNR) also demonstrate better matches with observational element abundances when the explosion models assume mild asymmetries (Nagataki 2000). Furthermore, recent observations of iron and silicon X-ray line emission (obtained with Chandra) exhibit clear morphological evidence of global asymmetries in the distributions of these elements within the Cas A SNR (Hwang et al 2004).

Finally, an equally compelling argument for global asymmetry arises from attempts to understand the high space velocities of neutron stars. The high observed velocities of pulsars and the formation scenarios of neutron star binaries both suggest that neutron stars

²A caveat to keep in mind for this argument is that alternative mechanisms for obtaining redshifts at infrared wavelengths do exist. In particular, Witteborn et al. (1989) showed that electron scattering effects from a homologously expanding envelope (at relatively low optical depth ~ 0.4) were capable of matching the redshifted lines of [ArII] (which exhibited similar features to the [FeII] line).

are given strong kicks at birth. These kicks are most easily explained by some asymmetry in the supernova explosion (see Fryer, Burrows, & Benz 1998 for a review). Observations of the pulsar shaping the guitar nebula place its proper motion measurement in excess of ~ 1000 km/s for the neutron star (Chatterjee & Cordes 2002). While its velocity places this neutron star near the high end of the observed pulsar velocity distribution, it is not off the charts. The distribution of pulsar birth velocities is bimodal, with peaks at 90 km/s and 500 km/s, where each peak represents roughly 1/2 the total population (Arzoumanian et al. 2002).

While the neutron star velocities and the spectral data both argue for the presence of a global explosion asymmetry, theoretical studies tell us that the origin of the asymmetries may not be related. Many kick mechanisms do not necessarily require asymmetries in the explosion itself (e.g. the neutrino driven mechanisms of Arras & Lai 1999; Fryer 2004). Conversely, the bipolar explosions produced by Fryer & Heger (2000) can explain some of the observed extended mixing in SN 1987A (HFW03) and may even explain the asymmetric appearance of Cas A (Hwang et al. 2004). However, they can not explain high neutron star velocities.

Scenarios capable (in principle) of generating kicks and ejecta asymmetries simultaneously do exist, though. In fact, the first multi-dimensional calculations of the collapse of a massive star to an explosion motivated just such a mechanism. Herant et al. (1994) argued for the importance of convection in enhancing the conversion of neutrino energies into kinetic explosion energy. One year later, Herant (1995) argued that if the convective cells could merge into one uprising bubble and one downflow, the explosion ejecta would be sufficiently asymmetric to explain neutron star kicks. Recent instability analyses by Blondin et al. (2003) and full core-collapse calculations by Scheck et al. (2004) have shown that such low mode convection may well be possible. In particular, Scheck et al. (2004) found that asymmetries arise naturally within the standard model of convective, neutrino-driven supernovae if the explosion is sufficiently delayed. They find uni-polar or single-lobe asymmetries capable of imparting kicks from 0 km/s to 1500 km/s.

The range of explosion asymmetries which result in neutron star kicks of this magnitude appear relatively mild (i.e. the explosion energies along the single-lobe are a few times larger than those in the remaining parts of the star.) This is in contrast to the explosion asymmetries in the magnetic, jet-driven supernovae proposed by Khokhlov et al. (1999), where all of the energy in the explosion is injected along a bipolar jet-axis. Wang et al. (2001) have argued that such mild asymmetries are unlikely to produce the global density asymmetries needed to generate the observed polarization. Parameterized 2D models of core explosions (carried out by Chevalier & Soker 1989) also show a tendency for explosion

asymmetries to spherize as the shock travels through the shallow density gradient in the hydrogen envelope of a SN Type II progenitor. Since polarization is observed to be a general property of core-collapse supernovae (both in Type II and Type Ib/c events), it is important that global density asymmetries persist through shock breakout even in progenitors with massive hydrogen envelopes (which stellar evolution models show to be the most common SN progenitor type.)

In this paper, we address both the issue of lopsided ejecta, and the persistence of global density asymmetries in the explosion of a *standard* supernova progenitor. This provides a baseline study upon which future work focussing on specific progenitors (e.g. as determined from observations of SN 1987A, Cas A) can build. We extend the work of HFW03 by concentrating on single-lobe explosion asymmetries and their effects on supernova observations. Our implementation of these single-lobe explosions is guided by 1) the magnitude of the velocity asymmetry and 2) the angular profile of the velocity asymmetry obtained from realistic models of core-collapse supernovae (Fryer & Heger 2000; Scheck et al. 2004). Specifically, we show that redshifted γ -ray lines can be produced entirely with the low-mode velocity asymmetries currently present in numerical core-collapse models (Scheck et al. 2004). Furthermore, the steep angular profile in velocity for these asymmetries allows global density asymmetries to persist even after the shock passes through the envelope of our red supergiant (RSG) progenitor model. This results in ejecta morphologies that are reminiscent of those observed in the Cas A SNR. Since we do not study the specific progenitors of SN 1987A or SNR Cas A, we can not say definitively that the current asymmetries in core-collapse calculations will explain the observations of these objects. However, these simulations do provide ejecta structures which could be used as the building blocks to construct the specific features seen in SN 1987A and SNR Cas A observations.

In §2, we present our asymmetric explosion calculations along with the numerical schemes and initial conditions used for those calculations. In §3, we discuss the effects such asymmetries have on the nuclear yields from these supernovae. Our calculations of the high energy (X-ray and γ -ray) emission and the resulting observations are presented in §4. We conclude with a discussion of the application of these calculations to supernova asymmetries observed in SN 1987A and SNR Cas A (including a discussion listing future work that will truly determine the efficacy of convection asymmetries in explaining the observed asymmetries in these objects).

2. Explosion Simulations

For our parametric study of single-lobe explosion asymmetries, we use the same $15 M_{\odot}$ progenitor star (s15s7b2 from Weaver & Woosley 1993) used in HFW03. We also model the explosions using the same incarnation of the 3-dimensional SNSPH code (Fryer & Warren 2002) used in HFW03 with only a few modifications described below. Low mode asymmetries in the explosion will lead to lopsided nickel distributions and may also alter the synthesis of nickel due to the angular variation in explosion energy. Because we start our simulations 100s after the launch of the explosion, no further nuclear burning occurs, and we can only estimate the possible effects asymmetric explosions might have on the actual synthesis of the ejecta elements. Instead, the simulations presented here concentrate on the hydrodynamic mixing of these elements.

2.1. Numerical Schemes

Roughly 1.2 million variably massed particles are used in the SPH simulation. Instead of using a grid of smooth particle hydrodynamics particles (HFW03), the neutron star (with mass of $1.4 M_{\odot}$) is cut out of the simulation. Its gravitational effect is mimicked with a central gravitational force term³. This reduces the numerical noise in the core and relaxes the Courant constraint on the timestep. As with the bipolar asymmetries, the single lobe asymmetry is imparted by artificially altering the explosion velocities at 100s after bounce. These input asymmetries require a factor by which the velocity is enhanced and an angular profile describing the assumed structure of the asymmetry. In HFW03, the angular dependence of the imposed velocity asymmetry was chosen to be sinusoidal. Their decision was made primarily to facilitate closer comparison with the results of Nagataki (2000) who also assumed this smoothly varying cosine behavior. Comparing with the 2D rotating collapse simulations of Fryer & Heger (2000) and the single lobe simulations of Scheck et al. (2004), we find that a sinusoidal velocity profile is probably smoother than the actual profiles in the hydrodynamic models. Figure 1 shows the SPH particle velocities from Fryer & Heger (2000) with a sinusoidal fit overplotted. A top-hat, with its sharp

³This is not a self-consistent treatment as the neutron star will have some velocity associated with it in order to conserve momentum in these one-sided explosions. The ejecta which are important for our γ -ray studies are homologously expanding with velocities greater than the escape velocity within a few weeks after the explosion is launched. The fastest moving neutron star in our simulations has a position offset from the center of the ejecta of roughly 20% the radius. This does not significantly affect the outflow trajectory of the ejecta that has already received escape velocity. In addition, this offset corresponds to material not yet probed by the escaping γ -ray emission, and can be neglected for this epoch ($t=365$ d).

transition, represents the other extreme in fitting the asymmetries from the explosion models (Figure 1). As we will discuss in the next section, a flat velocity profile in angle along the enhanced explosion axis significantly affects the outward mixing of nickel. While the steep transition of the top-hat profile may be more extreme than the numerical models, the existence of a flat-topped velocity profile (over polar angles of roughly 20 degrees) is likely more realistic than the sinusoidal profiles given the current core-collapse model results (Scheck et al. 2004; Fryer & Heger 2000).

Our set of single lobe explosion asymmetries are created assuming the discontinuous top-hat distribution, which represents a conical geometry and can be described by two primary parameters: 1) Θ = opening angle of the enhanced explosion cone, and 2) f = ratio of in-cone velocity to the corresponding out-of-cone velocity (the model names are meant to reflect these parameters; e.g. model f2th20 has $f = 2$, $\Theta = 20$). The in-cone and out-of-cone radial velocities are determined by keeping the same kinetic energy as the symmetric explosion while forcing f to a chosen value. They are given by:

$$V_{in-cone} = f \left[\frac{1 - f^2}{2} \cos(\Theta) + \frac{1 + f^2}{2} \right]^{-\frac{1}{2}} V_{symm} \quad (1)$$

and

$$V_{out-of-cone} = \left[\frac{1 - f^2}{2} \cos(\Theta) + \frac{1 + f^2}{2} \right]^{-\frac{1}{2}} V_{symm} \quad (2)$$

where V_{symm} is the radial velocity from the input 1D calculation.

Table 1 lists the suite of simulations studied in this paper. We have focused on an opening angle of 20° , but include a symmetric model with identical neutron star set-up for comparison. Additionally, a $\Theta=40^\circ$ model was run to get a rough impression of the dependence on opening angle. We have also included two simulations where the ^{56}Ni abundance has been enhanced by 100% within the opening angle. This corresponds to the maximum increase in the ^{56}Ni abundance seen in super-energetic explosion calculations (Hungerford et al. 2004). Because the opening angles are small, this enhancement corresponds to an increase in the total ^{56}Ni abundance of less than $\sim 10\%$.

As mentioned above, our choice of parameter values for this study are guided by the multi-dimensional simulations of Scheck et al. (2004) and Blondin et al. (2003), which find low mode instabilities driving the SN explosion. These calculations have found that low-mode instabilities can produce kick velocities ranging from 100 kms^{-1} and 1700 kms^{-1} .

Although our simulations also assume a range of kick velocities from 0-1690 kms^{-1} , our simplified models (both the single-lobe explosion and top-hat transition function) do not model the full range of results produced by the Scheck et al. (2004) and Blondin et al. (2003) calculations. The simulations in this paper are meant to give a flavor of what we can expect from asymmetries. A more thorough study of the range of asymmetric effects on the mixing will be presented in a later paper.

2.2. Explosion and Nickel Distribution

Figures 2 and 3 show the ^{56}Co distribution (isosurfaces of number density set to 10^{-5}) within the density distribution of the exploding star (shading) for the f3th40 and f2th20 models. These figures show the global view of the ejecta morphologies which develop from two extremes in our set of parameterized explosions. In particular, it is clear that the density asymmetries (shading) in both of the single lobe explosion models are much more extreme in these simulations than for the bipolar explosions of HFW03 (see their Fig. 5). The 3:1 velocity asymmetry of model f3th40 is sufficient to push through the entire star, creating a spray of heavy elements at the outermost edge of the expanding ejecta. Even the 2:1 velocity asymmetry in model f2th20 leads to aggressive outward mixing of nickel and its decay products, placing them very near the edge of the stellar ejecta as well.

The peak magnitudes of these velocity asymmetries do not differ significantly from those of the bipolar explosions in HFW03, but the outward mixing of the ^{56}Co is much more extensive than HFW03 found in their bipolar explosions. This is primarily due to the difference between the angular profiles of the velocity asymmetry. As mentioned above, the bipolar explosions were given a smoothly varying cosine velocity asymmetry, while the single lobe explosions assume a discontinuous “top-hat” profile in polar angle. The flat angular profile in the velocity for these single lobe models allows a significant portion of the high velocity region to expand without drag from fluid shear forces. This likely the cause of the increased heavy element penetration in the single lobe explosion models, rather than any differences in the geometry of the asymmetry. That said, results from current core-collapse models show that such flat-topped profiles in angle do exist over polar angles of 20 to 40 degrees (Figure 1; also see Figure 2 in Scheck et al. 2004).

A more quantitative look at the mass motions and energetics of the explosions can be seen in Figures 4 - 7 where the kinetic energy and mass are shown in cones with a 9° angular radius for a variety of polar angles in the f2th20 and f3th40 explosion models. The blue curve in each plot denotes the initial conditions of the model (100 s after launch of explosion), and the red curve is at later times when the ejecta flow has become homologous.

From the mass distributions, we see that the mass in the enhanced explosion lobe has increased while the mass at angles just outside the cone has been reduced. The in-cone material is shocked to higher velocities and expands rapidly, creating at its back a low density wake into which the surrounding material is funneled, thus increasing the total mass in the cone region at the expense of the material just outside the cone. This migration of material to the high velocity cone region affects the heavy element distribution as well, resulting in a larger mass of radioactive nickel within the cone. For the specific case of model f3th40, the enhanced explosion lobe is sufficiently energetic to poke a hole out of the star, spraying the matter from this cone in all directions. This leaves it with an overall enhancement in mass over the enhanced velocity cone, but actually results in a reduction of material right along the cone axis. The f2th20 model was not energetic enough to poke through the edge of the envelope, so it retains the mass enhancement over the entire cone region.

In conjunction with the mass distributions, the energy distributions show that a spherization of the explosion is taking place. While the mass in the cone has increased over time, the kinetic energy of the cone material has actually dropped off. This lost energy is spreading to the rest of the ejecta, equalizing the explosion velocities in angle. In the bipolar explosions of HFW03, the spherization of the explosion was essentially complete once the shock had passed through the star. For the explosions presented here, the peak velocity along the pole remains larger than the equatorial velocity, even after the shock has passed through the entire star. This velocity asymmetry gives rise to asymmetric density contours as shown in Figures 8 and 9 (blue contours in the left center panel) for models f3th40 and f2th20, respectively. Such persistent density asymmetries may be necessary to explain observations of supernova remnants. For instance, the morphology of SNR Cas A (with its optical jet) requires a density asymmetry that survives not just propagation through the star, but even significant interaction with the interstellar medium⁴.

While our chosen velocity asymmetries seem to reproduce features from remnant morphology, high energy line and continuum observations from SN 1987A possessed trends (broad lines, early detection of continuum) that must also be reproduced by these extended mixing structures. A first order test of the adequacy of this mixing is to compare our theoretical nickel distributions, plotted against line-of-sight velocity, with features in the observed infrared line profiles. Haas et al. (1990) argued that the [FeII] line profile reflects the entirety of the spatially distributed radioactive nickel, as any optically thick component of iron is likely distributed throughout the ejecta in clumps. The panels in Figures 8 and 9

⁴Keep in mind that it is also possible that the remnant asymmetries are caused by interaction with the circumstellar medium and have little to do with the explosion mechanism itself.

show nickel distributions versus line-of-sight velocity for models f3th40 and f2th20 at a variety of viewing angles as indicated by the black direction vectors. In addition, the distributions for the set of fXth20 models are plotted in Figure 10 for the anti-polar and equatorial viewing angles. For all these plots, the broadest line profiles are obtained when looking along the axis of the explosion asymmetry, though the range in profile shapes is quite large. Models f5th20 and f3th20 possess redward wings which do result in broadened line profiles (relative to the Symmetric model) as suggested by SN 1987A data. The f3th40 and f2th20 show relatively narrow line cores, however, they both possess a bump containing a few percent of the total nickel mass at high velocity. This high velocity component is particularly interesting as such a “bump” was invoked to explain irregularities in the H- α line observations of SN 1987A (i.e. “the Bochum event”).

The extended mixing in these simulations is also reflected in the spatial distribution of individual elements. Figure 11 shows plots of ^{56}Ni (top panel) and ^{44}Ti (bottom panel) versus enclosed mass for our suite of explosion models. Note that 3-dimensional mixing in our symmetric explosion places some nickel right up to the helium layer, well beyond the inner layers of the ejecta. In the asymmetric simulations, this mixing is much more extreme, placing nickel out to the outer layers of the star with a hundredth of a solar mass or more of nickel mixed into the hydrogen layer! If we assume that the inner 3-5 M_{\odot} falls back to form a black hole, we still eject $\sim 0.01\text{-}0.03 M_{\odot}$ nickel to power a weak supernova explosion⁵. If this much fallback occurred in our symmetric explosions, no nickel would be ejected and the optical display from this explosion would be too weak to be observed. Optical displays from systems that we believe form black holes are a sure sign of supernova asymmetry.

3. Abundance Enhancements

In §2.2, we showed how asymmetries can mix out the nickel formed in the explosion, transporting some of this nickel from the depths of the star well into the hydrogen envelope. Asymmetries in the explosion energy can also alter the abundance of elements synthesized in the explosion. Because we do not start our simulations until 100 s after the launch of the explosion, we can not directly calculate the yields from these explosion asymmetries. But we can estimate the effect of asymmetries on the element synthesis by combining the results from 2 separate 1-dimensional simulations to mimic both the strong conical burst and the

⁵Bear in mind that in our simulation, starting 100 s after bounce, there is very little fallback. To really determine the mixing for an explosion with this much fallback, we would need to model an explosion with weaker energies starting at earlier times. Plans for such calculations are underway.

remainder of the star. For this estimate, we use the 1-dimensional explosions of a $15 M_{\odot}$ star from (Hungerford et al. 2004, 2005). In the most extreme case (our f5th20 model), the energy within the lobe corresponds to a spherical explosion of $\sim 15 \times 10^{51}$ ergs (although its 1% total volume means that it contributes only 1.5×10^{50} ergs to the total explosion energy of this asymmetric outburst). The rest of the star has an effective spherical energy of roughly 0.6×10^{51} ergs.

For the f3th40 simulation, the energy within the lobe corresponds to $\sim 5 \times 10^{51}$ ergs, but the total volume is 10% and it is this model that will show the largest variation in nucleosynthetic yield from supernova asymmetries. Figure 12 (top) shows the abundance fraction (relative to solar) of stable isotopes as a function of isotope mass for 1-dimensional explosions with energies of 1.35×10^{51} ergs (black) and 6.5×10^{51} ergs (blue). The red data shows the linear combination (90% at 1.35×10^{51} ergs, 10% at 6.5×10^{51} ergs). The abundances are only slightly different than what we would expect from a 1-dimensional explosion with an energy of 1.35×10^{51} ergs.

For the strong explosions in this paper, the effect on the nucleosynthetic yields of stable isotopes is minimal. But the situation is very different for some radioactive yields. Let’s look at these yields in more detail.

- **^{56}Ni** : 0.014, 0.154, $0.37 M_{\odot}$ for 0.1, 1.35, 6.5×10^{51} erg explosions.
- **^{44}Ti** : $< 10^{-20}$, 1.3×10^{-5} , $1.4 \times 10^{-6} M_{\odot}$ for 0.1, 1.35, 6.5×10^{51} erg explosions.
- **^{26}Al** : $< 10^{-20}$, 3.4×10^{-10} , $4.3 \times 10^{-5} M_{\odot}$ for 0.1, 1.35, 6.5×10^{51} erg explosions.

Especially notice the yield of radioactive ^{26}Al . The ^{26}Al yields reported above do not include the hydrostatically synthesized contribution, however recent models from Limongi & Chieffi (2005) argue that explosive production of ^{26}Al dominates the total yield for a wide range of main sequence masses; this is particularly true at the lower masses like the 15 solar mass progenitor employed here. Our results show that the ^{26}Al synthesized during the explosion can be orders of magnitude higher in an asymmetric explosion than in a symmetric explosion of comparable total explosion energy. Depending upon the frequency and magnitude of explosion asymmetries, this enhancement may allow SN II to be the primary synthesis site for ^{26}Al , a possibility which had been ruled out based on theoretical yields assuming spherical symmetry (see Higdon, Lingenfelter & Rothschild 2004 and references therein). However, be aware that these estimates are at zeroth order, using many simplifications. A full calculation of the nuclear burning in the multi-dimensional, asymmetric explosions is needed to determine which aspects of these results will remain true. Still, it is interesting to note that the trends we see for ^{44}Ti and ^{26}Al in these 1D

models are contrary to those reported by other authors in the literature (Nagataki 2000 report increasing yields for ^{44}Ti with larger explosion energy and Limongi & Chieffi 2005 report constant yields for ^{26}Al with increased explosion energy.)

For our calculations, which focus on the γ -ray emission, the most important yield is that of ^{56}Ni and its decay product: ^{56}Co . For most of our calculations, we assume that the ^{56}Ni remains unchanged from the predictions of our progenitor model. But to test the extreme possible effect of our asymmetries on the γ -ray line profile, we have also included two simulations (f2th50enh, f3th40enh) that enhance the ^{56}Ni within the energetic lobe by a factor of two (Table 1). This corresponds to a total increase in ^{56}Ni by roughly $0.02, 0.2M_{\odot}$ for the $\Theta = 20, 40$ models respectively. We have added this ^{56}Ni from the inside out (to mimic the trends we see in our 1-dimensional calculations). The effect of this enhancement will be discussed in more detail in §4.

For weaker explosions, even the stable isotope yields can vary by over an order of magnitude. Figure 12 (bottom) shows the same abundance fractions with 1-dimensional explosion energies of 0.1×10^{51} ergs (black) where a lot of fallback occurs, 6.5×10^{51} ergs (blue), and the 90%,10% linear combination (red). Here the small, energetic outburst drastically alters the predicted yields of the star. Indeed, in this scenario, even though we would expect considerable fallback, the yield would be within a factor of a few for most elements with respect to normal supernova. We postpone study of these weak explosions to a future paper.

4. High Energy Spectral Calculations

We now turn to studying the effects these hydrodynamic asymmetries have on the γ -ray spectra and fluxes. In particular, we can test to see if one-sided explosion asymmetries can produce redshifts in the γ -line profiles. We concentrate our γ -transport simulation efforts primarily on the ejecta structures at a single time ($t = 1 \text{ yr}$)⁶, and investigate trends in the line centroid shift with viewing angle. As we mentioned before, the progenitor star used in these simulations differs appreciably from the best-fit progenitor to SN 1987A. This precludes us from directly comparing our theoretical line shifts to the γ -line observations of Tueller et al. (1990) and the observed [FeII] forbidden lines from Spyromilio et al. (1990) and Haas et al. (1990).

⁶We present a few simulations at earlier and later times to qualitatively investigate time evolution, though we defer a more rigorous study to a future paper.

4.1. Numerical Schemes

As with the previous simulations, our input models of the supernova ejecta (element abundances, density and velocities) are taken from the f2th20 and f3th40 SPH explosion simulations described above and mapped onto a $140 \times 140 \times 140$ Cartesian grid. Escaping photons were tallied into 250 coarse energy bins, with finer binning at the decay line energies to provide line profile information. The emergent photons were also tallied into 11 angular bins ($\Delta\theta = 10^\circ$). While the input data is not of an axisymmetric nature, the set of angles chosen are fairly representative of the overall structure.

Roughly 5×10^9 Monte Carlo photon bundles were generated for each input model, in proportion to the mass of radioactive material distributed throughout the ejecta. For these models, photoelectric and pair production opacities were calculated for the elements H, He, C, O, Ne, Mg, Si, Fe, Co, and Ni. These elements correspond to those used in the nuclear network by Timmes, Hoffman & Woosley (2000), which has been incorporated into the SPH code but was turned off in these calculations for computational efficiency. This reduction in the number of elements treated (relative to HFW03) manifests itself as variations in the spectral turnover at low energies, but does not affect the Compton scattered continuum as Y_e , and hence the electron density, is the same. As mentioned above, HFW03 used a grid of central SPH particles to represent the central neutron star. The treatment of particle composition when mapping to the Monte Carlo grid led to an overproduction of ^{56}Ni by roughly 35%. The simulations presented here replace the central SPH particles with an external gravitational force and do not suffer from the nickel overproduction. In all other aspects, the simulations remain the same as in HFW03.

4.2. Hard X-ray and Gamma-ray Spectrum

Without the benefit of a progenitor and explosion model tuned specifically to SN 1987A, it is difficult to draw meaningful conclusions regarding the continuum portion of the high energy spectrum. The hard X-ray continuum was detected earlier than theory predicted based on spherically symmetric (i.e. unmixed explosion models.) Multi-dimensional explosions, capable of modeling the mixing instabilities, have been simulated using a stellar progenitor appropriate for SN 1987A (Kifonidis et al. 2003; Nagataki 2000; Herant & Benz 1992). However, the nickel distributions from these globally symmetric explosion models were not broad enough to match the first order comparison against IR line profiles, so further modeling of the high energy spectrum was not performed. This work tells us that additional mixing (possibly arising from a global asymmetry) is needed to match the broad lines, but it tells us nothing regarding the effect a global asymmetry should have

on the continuum. The high energy spectra from a subset of our explosion simulations (using a generic red supergiant SN progenitor) are shown in Figure 13, where photon flux (phot/s/MeV/cm²) is plotted logarithmically across the energy range investigated with these simulations (0.3 keV - 4 MeV). It's clear that the asymmetric explosions produce a lower continuum relative to the symmetric explosion model, and that the time evolution of models with different input asymmetries is qualitatively different. Previous work has judged its mixing successes and failures based on the spatial distribution of nickel alone, however, these results suggest that the hard X-ray emission can vary widely with asymmetry type and high energy calculations are necessary for determining the adequacy of any SN 1987A mixing calculation.

4.3. Gamma-ray Line Profiles

Figures 14 - 18 show the 847 keV γ -ray line profiles for our suite of single lobe explosion models. The plots are the same layout and represent the same viewing angles as in Figures 8 and 9. These figures demonstrate that redshifted line profiles *are* attainable given the types of asymmetries assumed here. However, it is clear by comparing to Figures 8 and 9, for models f3th40 and f2th20, that the line profiles do not reflect the entirety of the underlying nickel distribution. Indeed, as argued in HFW03, the high energy emission can be understood by assuming that the emission at all viewing angles is dominated by the extremities of the nickel distribution (which has mostly decayed to cobalt at this epoch.)

Each energy bin in the Doppler broadened profile can be mapped to a spatial location in the ejecta. This is due to the homologous nature of the expansion, in which line of sight velocity is proportional to line of sight distance from the mid-plane of the explosion. Keeping this in mind, one can use the structure of the cobalt contour plots in Figures 14 - 18 to understand the line profiles plotted in the surrounding panels. Each energy bin in the line profile corresponds to emission from all the cobalt located along a line perpendicular to the viewing angle vector (black line drawn from explosion center to line profile panel.)

In particular, for the f3th40 model, the base of the antenna-like structures is the primary emission site for γ -rays that escape at all angles. For the $\theta=0$ direction, this leads to a blue shifted line with a long blue wing contributed by photons from the antenna structures themselves. The $\theta=90$ direction shows two separate peaks with emission shoulders to the red and blue. The peaks arise from the structure just at the split of the two antennae, with the near side giving rise to the slightly blueshifted peak and the far side making up the slightly redshifted peak. The shoulders on these peaks arise from the emission of the antenna material. The same correspondence between the outlying cobalt

distribution and line profile structure can be made for the f2th20 model. In each panel there is a small contribution from the mildly blueshifted material at the outer edge of the spherical structure in the center. However, for the viewing angles with a clear view to the cylindrical structure along the z-axis, the profiles are dominated by that emission. In particular, the $\theta=0$ direction shows a strongly blueshifted peak from the spray at the end of the cylinder and a shallow redward wing from the emission of the cylinder itself. In the $\theta=90$ direction, the high z-velocity material in the cylinder has a low line of sight velocity and gives an emission peak at roughly the rest frequency. However, this profile does show extended red and blue wings arising from the spray at the end of the cylindrical structure. The simulations with enhanced nickel synthesis, show little difference from the standard simulations, primarily because the enhancement affects the inner nickel distribution most strongly, while the γ -ray lines are most sensitive to the outwardly mixed nickel.

While it is encouraging that such a line shape can be reproduced at all, it is important to note that in both models the redshifted line shape comes at the expense of line flux. We see significant redshifts because we see only a fraction of the radioactive emission which has been mixed out to low densities in the ejecta (and thus low opacities.) Indeed, the integrated flux for any viewing angle in the 847 keV line represents only a few percent of the total flux from the $0.24 M_{\odot}$ of nickel ejected in these models. The γ -line observations of SN 1987A implied 20% escape fraction at roughly 400 days (Tueller et al. 1990), however the explosion energy for SN 1987A was likely larger than that of our simulations (Woosley 1988). As a result, we would expect the timescales for uncovering the radioactive nickel to be different in SN 1987A so as to account for the larger escape fraction. However, for the models considered here, a larger escape fraction would mean a more significant contribution from the spherically distributed nickel deeper in the ejecta, possibly washing out the redshift in the observed profile.

In order to probe the effect a larger escape fraction might have on the overall γ -ray lineshifts, we look to later times in the evolution of the f2th20 and f3th40 explosion models. Figures 14 and 15 show the 847 keV ^{56}Co line profiles for $t = 250$ and 600 days overplotted with the profiles at 1 year. There is a clear evolution with time of the line centroid. As the ejecta expand, the “observed” line profile shifts toward the decay rest energy regardless of viewing angle. So we find that these particular models seem to have difficulty reproducing the time independence of the redshifted line profiles in SN 1987A. However, these simulations also suggest that the general nature of the extended nickel distribution varies sensitively with assumed velocity asymmetry. One can imagine that it is possible to reconstruct the specifics of the SN 1987A observations with an appropriately distributed “spray” of radioactive nickel products. There remain many “ifs” regarding the ability of this mechanism to match the line fluxes and time evolution of the γ -ray lines of SN 1987A.

However, the outlook is good that this may be the solution we have been looking for and a serious effort to match the SN 1987A data specifically using asymmetries of this nature is definitely warranted. For the specific explosion parameters assumed here, we can already conclude that the asymmetry in the explosion manifests itself most clearly in the “spray” of heavy elements along the enhanced explosion lobe. It is the detailed structure of this nickel “spray” that is directly probed by the γ -ray line profiles at this epoch, thus probing the material most likely to indicate a break in global symmetry.

5. Summary

The hydrodynamic simulations investigated here probe only a small portion of the large parameter space for explosion asymmetries. From this limited sample we can say that the outward mixing of heavy elements in these single lobe explosion models is more extended than the bipolar explosion simulations of HFW03. The differences in adopted angular profile of the imposed velocity asymmetry is likely responsible for this enhancement, rather than the difference between bipolar and single lobe explosion geometry. The overall morphologies in the high f explosions (f5th20, f3th20 and f3th40) are particularly reminiscent of the Cassiopeia A supernova remnant, in that the heavy element distribution shows a clear “jet” blowing out of the star. The persistence of such a density asymmetry through the extended envelope of our RSG progenitor is promising, primarily for matching the polarization observations in Type II SNe. It is also heartening that remnant morphologies like Cas A can be achieved through explosion asymmetries, though this is less crucial since it is entirely possible that stellar wind profiles and binary interactions have a larger affect on the remnant structure than the explosion mechanism.

The high energy transport simulations, which are calculated as a post-process on the hydrodynamic models, verify that redshifted line profiles are attainable for γ -ray decay emission in single lobe explosion asymmetries. However, the redshifted emission is primarily attributed to the “spray” regions of enhanced outward mixing of cobalt. This means that the specifics of the γ -ray line profiles are strongly tied to the structure of the hydrodynamic mixing and do not probe the entirety of the nickel distribution. This is extremely fortunate, as it is this outlying material that contains the most information regarding the initial velocity asymmetry. In this way, the combined sensitivity of the γ -rays to the “spray” material, and the “spray” material to the underlying velocity structure, make the γ -rays an ideal probe of the explosion mechanism itself. This begs the question, what is the likelihood of detecting the γ -ray line emission from core-collapse supernovae with current and future γ -ray instruments? Observations at these high energies require space observatories, or

at the very least, high-altitude balloon missions. The current state-of-the-art for γ -ray observations is the International Gamma-Ray Astrophysics Laboratory (INTEGRAL, operated by European Space Agency). A caveat to keep in mind is that the nickel mass synthesized in this $15 M_{\odot}$ model is roughly 2 times larger than the mean observed value ($\sim 0.13 M_{\odot}$; Hamuy 2003) for core-collapse SN explosions. However, as mentioned earlier, the explosion energy was roughly half that of a normal supernova. These two effects serve to balance one another, though it is difficult to determine the exact effect as nickel distributions and optical depth profiles are not simply described.

At energies around 1 MeV, INTEGRAL will have a spectral resolution of 2 keV and a narrow line sensitivity (3σ in 10^6 seconds) of $\sim 5 \times 10^{-6}$ phot $s^{-1} \text{ cm}^{-2}$ (Hermsen & Winkler 2002). Our model lines are about 5 times broader than this resolution element, so the sensitivity for detecting them is worse by roughly $\sqrt{5}$. Using these specifications, INTEGRAL would be able to detect the ^{56}Co lines from the single lobe explosion models (looking along the explosion lobe) at a distance of roughly 850 kpc and 300 kpc for the f3th40 and f2th20 models respectively. Table 5 shows the luminosities for various continuum energy bands and line energies from the four asymmetric models studied here (f2th20, f3th20, f5th20 and f3th40). At these distances (less than a Mpc), the occurrence rate for core-collapse supernovae is essentially the rate for a Galactic event (roughly 1-2 per century; Cappellaro et al. 1993). For a Galactic supernova event, INTEGRAL would be able to measure not only line flux but line profile information, allowing the full diagnostic potential of the γ -rays to be tapped.

While the signatures of asymmetry in any one of our models do not exactly match the specific observations of SN 1987A or Cas A SNR, the set of simulations in HFW03 and this work seem to span the range of observed features. For our most extreme velocity asymmetries, we see “jet”-like morphologies in the ejecta density plots and iron group elements mixed to the outer edge of the SN ejecta. Redshifted line profiles can be seen along certain viewing angles in the single lobe explosions, as can broadened line profiles. In addition, the discontinuous velocity asymmetry in these single lobe explosions produces high velocity nickel clumps, an important ingredient in the explanation of SN 1987A’s Bochum event. Finally, the single lobe explosions seem to result in dimmer continuum emission relative to the symmetrically mixed explosion models. We note that the smoother, bipolar explosion model in HFW03 shows an enhancement in continuum emission and results in even broader line profiles than are seen in these single lobe explosion models.

An important ramification of these results is that features associated with ejecta asymmetry are reproduced naturally within the context of the standard neutrino driven supernova mechanism. Our input parameters were motivated by the core collapse

simulations of Scheck et al. (2004)⁷, in which neutrino driven convective motions are responsible for the explosion asymmetry⁸. The simulations presented in this paper, and in HWF03, suggest that a combination of the bimodal and unipolar asymmetries may well explain all the observable features of SN 1987A or Cas A SNR. *No jet-induced explosion need be invoked for these, and indeed, most supernova explosions.* Without knowing it, Fryer & Warren (2004) already produced such a combination in the explosion of a rotating star (model SN15B). Obviously, a convincing demonstration of this awaits the simulation of a progenitor model specific to SN 1987A or Cas A SNR and a more comprehensive study of the asymmetries. But the pieces are now on the table and we plan to continue with more object specific studies to convincingly solve this puzzle.

This work was funded under the auspices of the U.S. Dept. of Energy, and supported by its contract W-7405-ENG-36 to Los Alamos National Laboratory, by a DOE SciDAC grant number DE-FC02-01ER41176 and by NASA Grant SWIF03-0047-0037. The simulations were conducted on the Space Simulator at Los Alamos National Laboratory.

⁷Likewise, the input asymmetry in HFW03 was motivated by core collapse calculations of Fryer & Heger (2000).

⁸A caveat to keep in mind is that the asymmetry inferred from the collapse simulations is not imposed onto the ejecta until the shock has nearly reached the hydrogen layer. However, the shock primarily accelerates until it reaches this layer and any velocity asymmetry is likely to persist until this point.

Table 1. Summary of Simulations

Model	Θ	f	$v_{\text{kick}}(\text{kms}^{-1})$
symm	0	1	0
f2th20	20	2	320
f2th20enh ^a	20	2	320
f3th20	20	3	600
f5th20	20	5	1010
f3th40	40	3	1690
f3th40enh ^a	40	3	1690

^aAbundances enhanced by increasing the total ⁵⁶Ni abundance by $\sim 100\%$ inside the cone.

Table 2. Line and Continuum Fluxes

Model	3-30 keV (erg s ⁻¹)	30-100 keV (erg s ⁻¹)	100-500 keV (erg s ⁻¹)	847 keV Line (γ s ⁻¹)	1238 keV Li (γ s ⁻¹)
f2th20	6.133(0.080) × 10 ³⁷	2.731(0.065) × 10 ³⁸	9.929(0.394) × 10 ³⁸	3.087(0.144) × 10 ⁴⁴	2.614(0.176) × 10 ⁴⁵
f3th20	7.626(0.095) × 10 ³⁷	3.182(0.073) × 10 ³⁸	9.848(0.413) × 10 ³⁸	1.078(0.109) × 10 ⁴⁴	2.348(0.199) × 10 ⁴⁵
f5th20	5.331(0.101) × 10 ³⁷	2.719(0.088) × 10 ³⁸	8.698(0.496) × 10 ³⁸	0.790(0.112) × 10 ⁴⁴	1.964(0.224) × 10 ⁴⁵
f3th40	2.882(0.055) × 10 ³⁷	2.611(0.067) × 10 ³⁸	16.45(0.521) × 10 ³⁸	1.023(0.030) × 10 ⁴⁵	9.531(0.348) × 10 ⁴⁵

REFERENCES

- Arnett, W. D., Bahcall, J. N., Kirshner, R. P., & Woosley, S. E. 1989, *ARA&A*, 27, 629
- Arras, P. & Lai, D., 1999, *ApJ*, 519, 745
- Arzoumanian, Z., Chernoff, D. & Cordes, J., 2002, *ApJ*, 568, 289
- Blondin, J., Mezzacappa, A. & DeMarino, C., 2003, *ApJ*, 584, 971
- Chatterjee, S., & Cordes, J. 2002, *ApJ*, 575, 407
- Dotani, T., Hayashida, K., Inoue, H., Itoh, M., & Koyama, K. 1987, *Nature*, 330, 230
- Fryer, C., Burrows, A. & Benz, W., 1998, *ApJ*, 496, 333
- Fryer, C. L., & Heger, A. 2000, *ApJ*, 541, 1033
- Fryer, C., & Warren, M. 2002, *ApJ*, 574, 65
- Fryer, C., 2004, *ApJ*, 601L, 175
- Grant, K. J. & Dean, A. J., 1993, *A&AS* 97, 211
- Haas, M. R., Erickson, E. F., Lord, S. D., Hollenbach, D. J., Colgan, S. W. J., & Burton, M. G. 1990, *ApJ*, 360, 257
- Herant, M., & Benz, W. 1992, *ApJ*, 387, 294
- Herant, M., Benz, W., Hix, W.R., Fryer, C.L. & Colgate, S.A. 1994, *ApJ*, 435, 339
- Herant, M., 1995, *SSRv*, 74, 335
- Higdon, J., Lingenfelter, R., & Rothschild, R. 2004, *ApJL*, 611, 29
- Höflich, P., 1991, *A&A*, 246, 481
- Hungerford, A.L., Fryer, C.L., & Warren, M.S. 2003, *ApJ*, 594, 390
- Hungerford, A. L., Fryer, C. L., Timmes, F. X. & McGhee, K. , submitted to *Nuc. Phys. A*
- Hungerford, A. L., Fryer, C. L., Timmes, F. X., in preparation
- Hwang, U., Laming, J.M., Badenes, C., et al. 2004, *ApJL*, 615, 117
- Kifonidis, K., Plewa, T., Janka, H.-Th., & Müller, E. 2003, *A&A* 408, 621

- Khokhlov, A., Höflich, P., Oran, E., Wheeler, J. C., Wang, L. & Chtchelkanova, A. Yu
1999, ApJL, 524, 107
- Leonard, D. C., & Filippenko, A. V. 2001, PASP, 113, 920
- Nagataki, S. 2000, ApJS, 127, 141
- Scheck, L., Plewa, T., Janka, H.-Th., Kifonidis, K., Müller, E., 2004, PhRvL, 1992, 011103
- Spyromilio, J., Meikle, W. P. S., & Allen, D. A. 1990, MNRAS, 242, 669
- Sunyaev, R., Kaniovskii, A., Efremov, V., Gilfanov, M., & Churazov, E. 1987, Nature, 330,
227
- Timmes, F., Hoffman, R. & Woosley, S., 2000, ApJS, 129, 377
- Tueller, J., Barthelmy, S., Gehrels, N., Teegarden, B. J., Leventhal, M., & MacCallum, C.
J. 1990, ApJ, 351, L41
- Wang, L., Howell, D. A., Höflich, P., Wheeler, J. C. 2001, ApJ, 556, 302
- Weaver, T. A., & Woosley, S. E. 1993, Phys. Rep., 227, 65
- Witteborn, F.C., Bregman, J.D., Wooden, D.H., Pinto, P.A., Rank, D.M., Woosley, S.E., &
Cohen, M. 1989, ApJL, 338, L9
- Woosley, S. E. 1988, ApJ, 330, 218

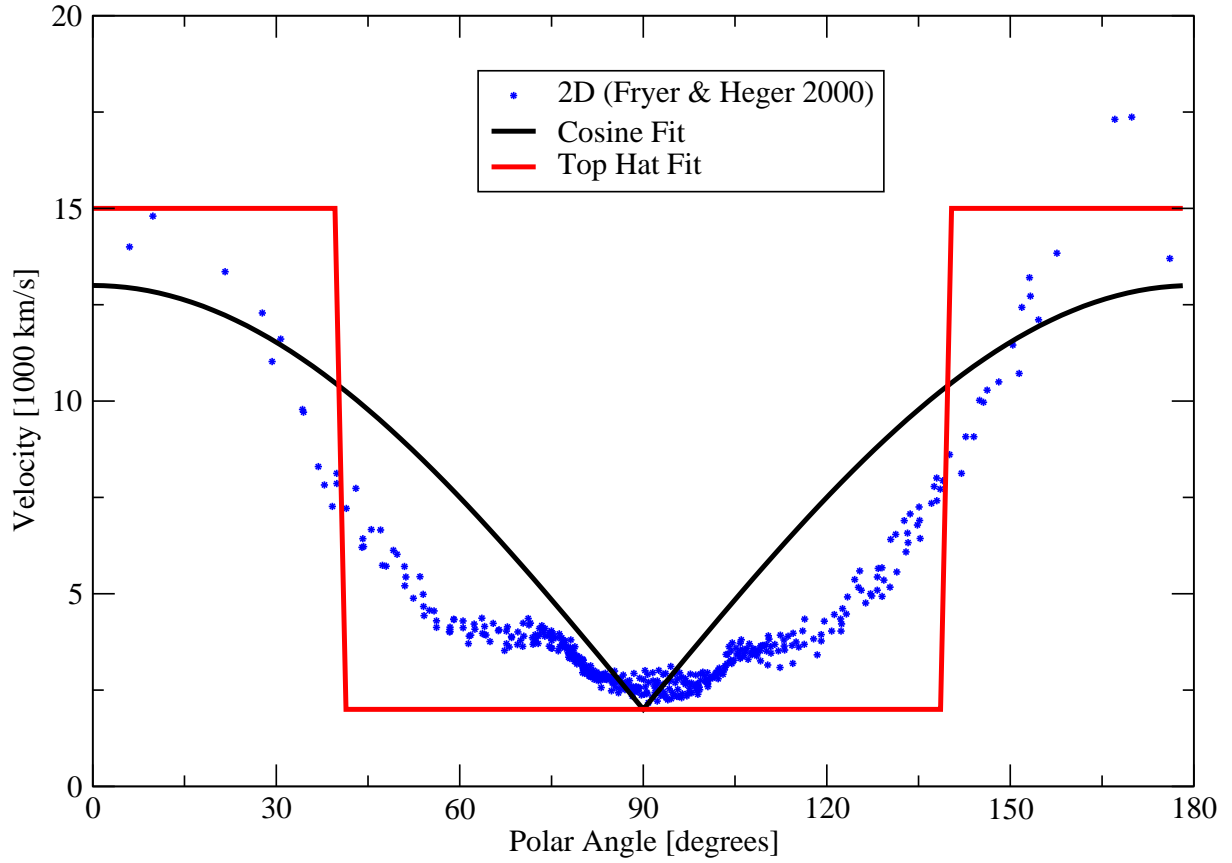


Fig. 1.— Plot of radial velocity versus polar angle for the 2D rotating collapse model of Fryer & Heger (2000). Overplotted are the cosine function used in HFW03 and the top-hat function to represent the profiles for the artificial velocity asymmetries. Note that the model profile lies somewhere between these two extremes.

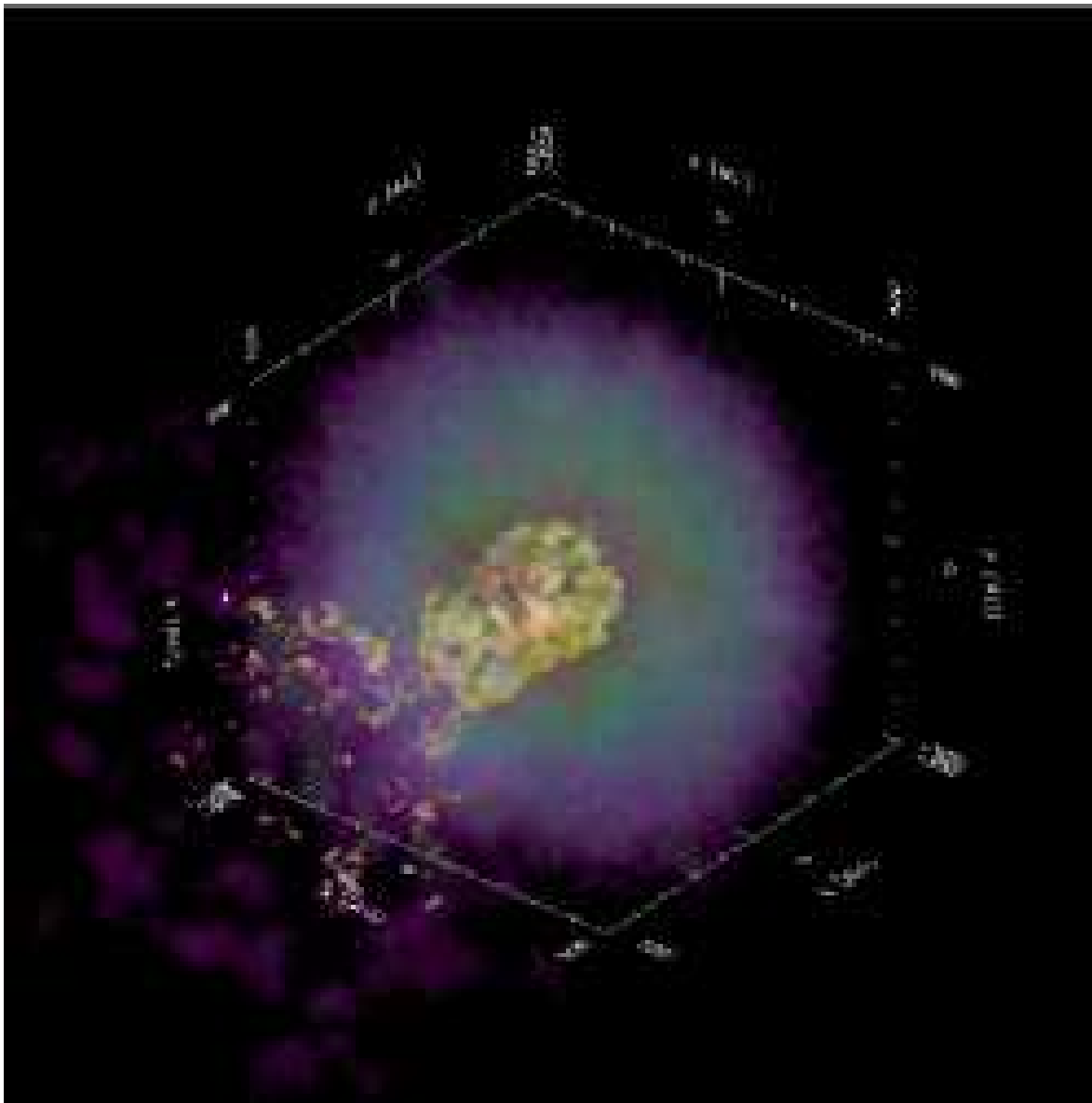


Fig. 2.— 3-dimensional rendering of the f3th40 explosion model 1 year after the shock launch. The isosurface represents the cobalt distribution with a number density of 10^{-5} . The colors denote the density distribution. The top-hat distribution of the imposed velocity asymmetry allows a significant portion of the cone material to expand without drag from fluid shear forces, resulting in the large splash of material at the outer ejecta.

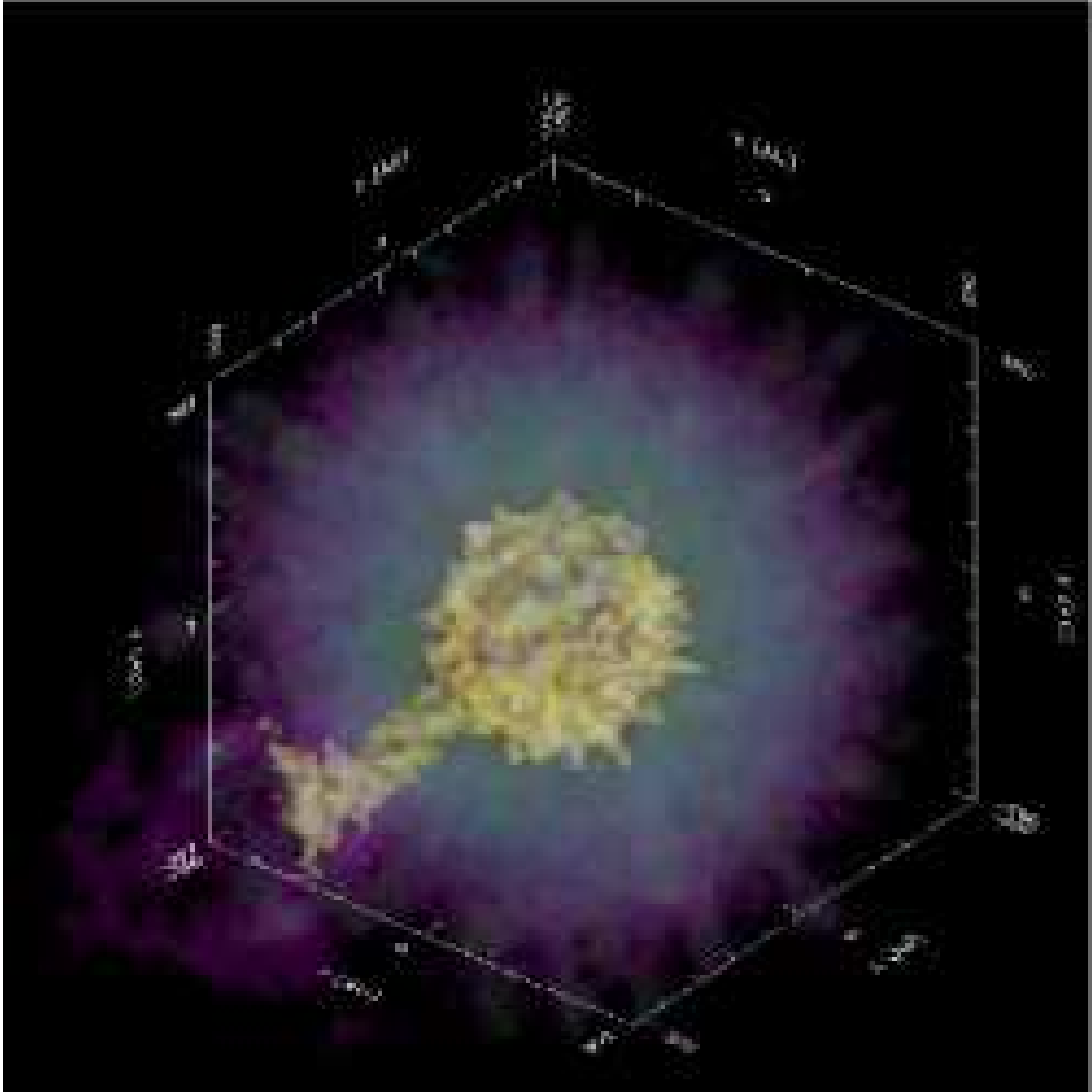


Fig. 3.— Same as previous figure, but for model f2th20. Again we see the splash of cobalt in the outer ejecta, but it is not as extreme because of the smaller angle and lower contrast of the velocity asymmetry.

Model f3th40

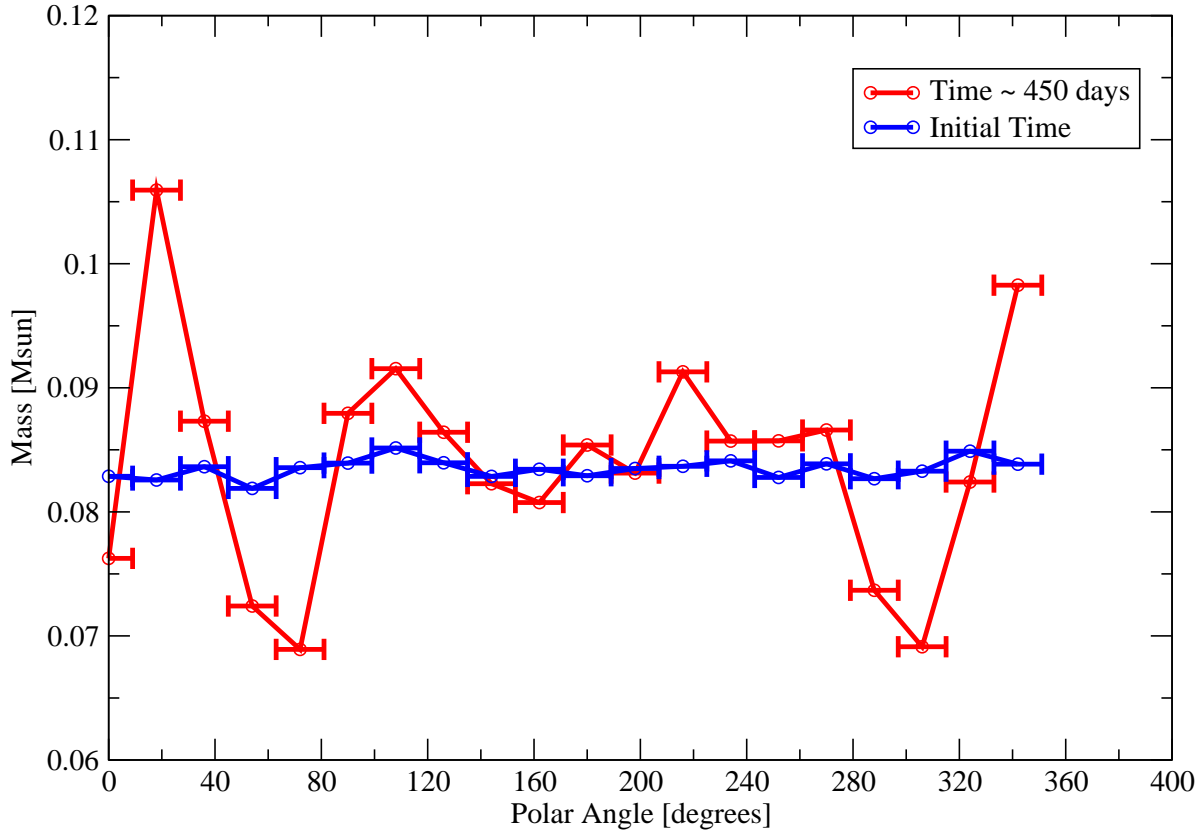


Fig. 4.— Plot of mass in a cone of radius 9° along a direction in polar angle for the f3th40 model. Error bars reflect the cone diameter. Blue line is for the initial time at $t = 100$ s and red line is for $t = 450$ days (long after flow has become homologous.) Matter is being funneled into the faster expanding, lower density region in the cone. This results in an enhancement of the mass for polar angles near zero, and a reduction in mass for angles just outside of this.

Model f2th20

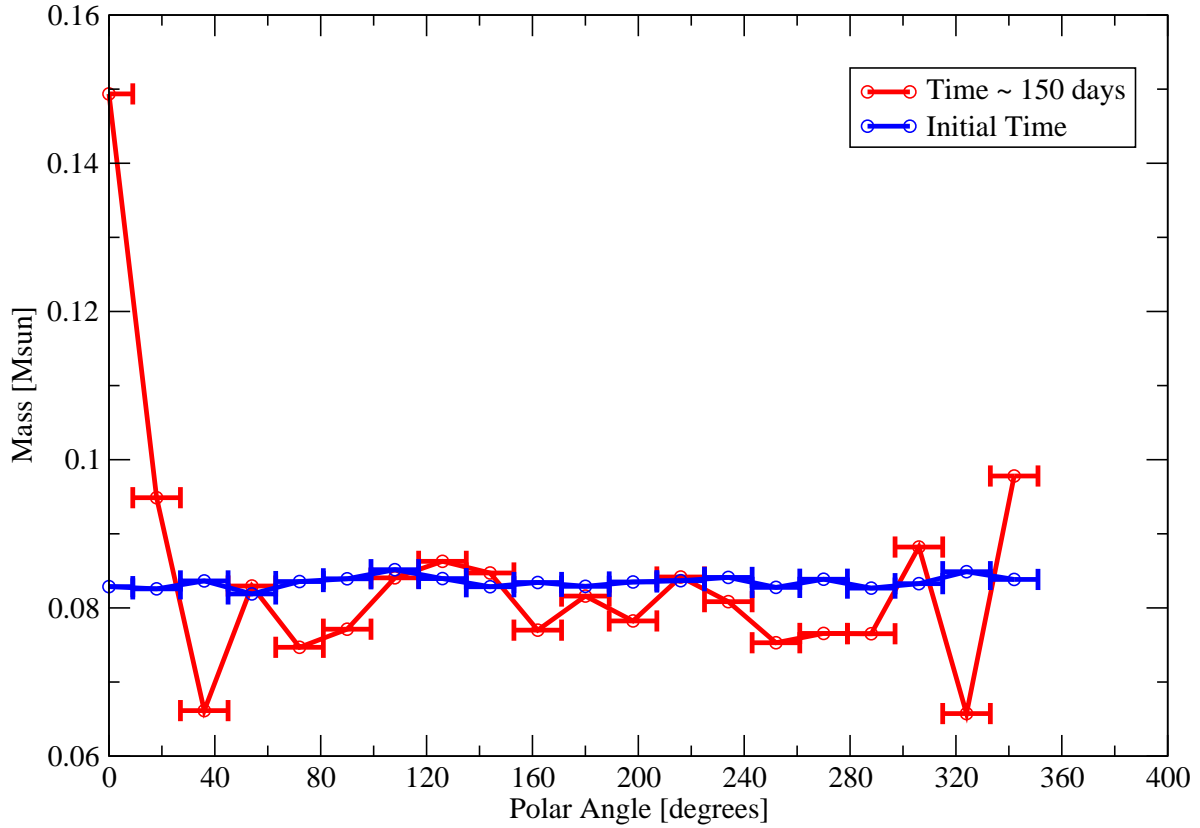


Fig. 5.— Similar to the previous figure, but for model f2th20 at $t = 150$ d. The ejecta have already reached the phase of homologous expansion, so can be directly compared with the f3th40 results.

Model f3th40

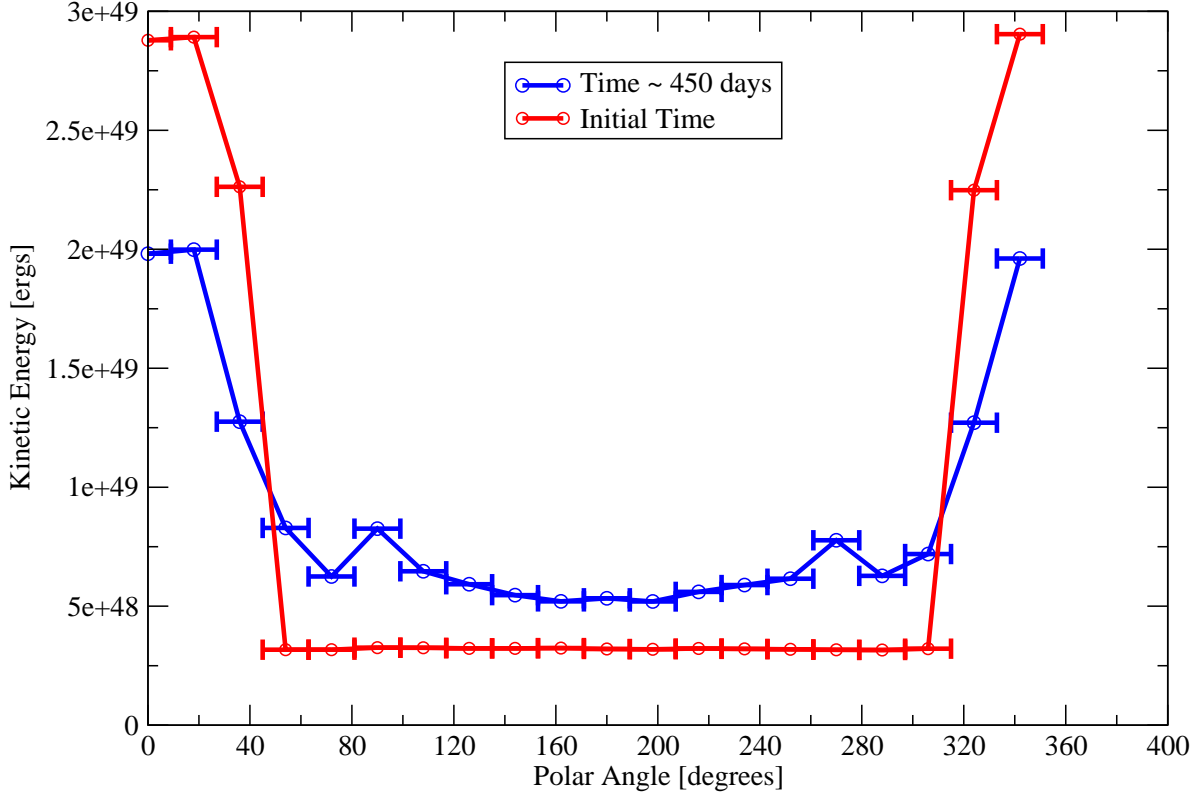


Fig. 6.— Similar to the previous figures, but showing kinetic energy as a function of polar angle for the f3th40 model. Blue line is for the initial time at $t = 100$ s and red line is for $t = 450$ days (long after flow has become homologous.) It is clear that the explosion is spherizing (i.e. energy in the enhanced explosion lobe is smearing and being shared with the rest of the ejecta.) Note from the previous figures that the mass in the cone actually increases at later times, suggesting that the velocity structure is even more spherical than the energy distribution shown here. Still, after having the shock pass through the entire star, there does still remain some asymmetry in contrast to the complete spherization of the bipolar explosion models.

Model f2th20

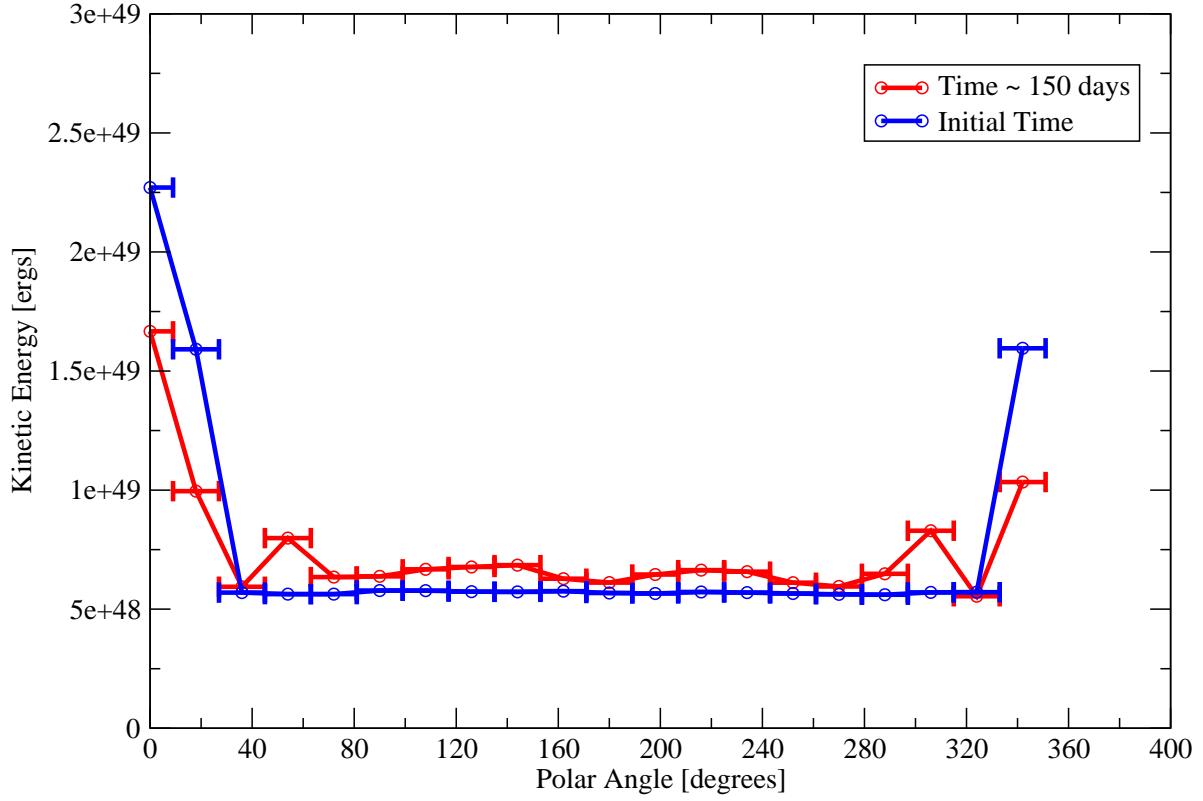


Fig. 7.— Similar to the previous figure, but for model f2th20 at $t = 150$ d. The ejecta have already reached the phase of homologous expansion, so can be directly compared with the f3th40 results.

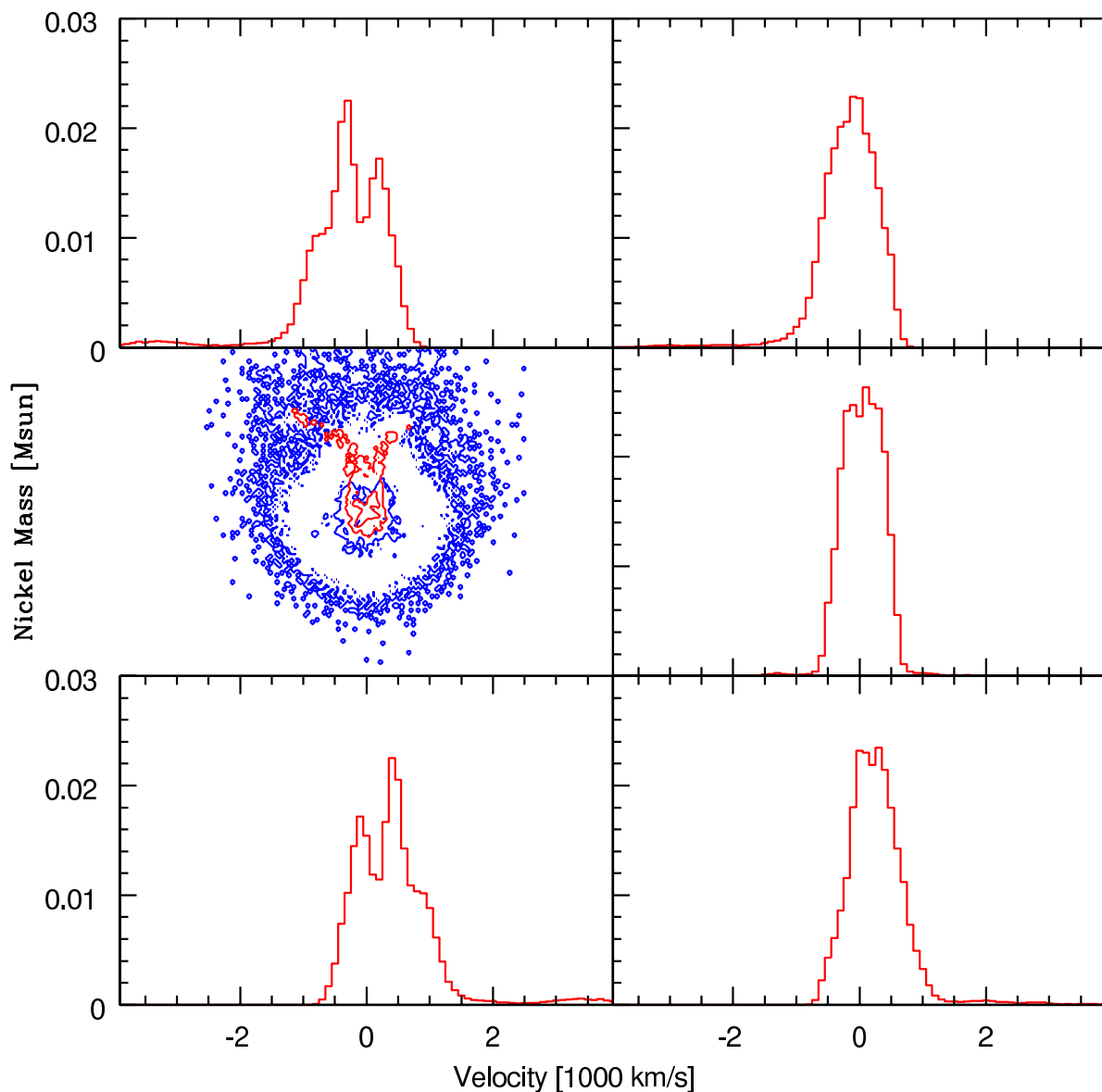


Fig. 8.— Mass of 56-weight elements (e.g. initial ^{56}Ni mass) versus line of sight velocity for a number of viewing angles in model f3th40 at $t = 365$ days. Central panel on the left shows a contour plot of density (blue) and cobalt number density (red). Due to the homologous nature of the expansion, these distributions represent the line shapes one would expect from nickel, cobalt or iron emission in the absence of significant ionization or opacity effects.

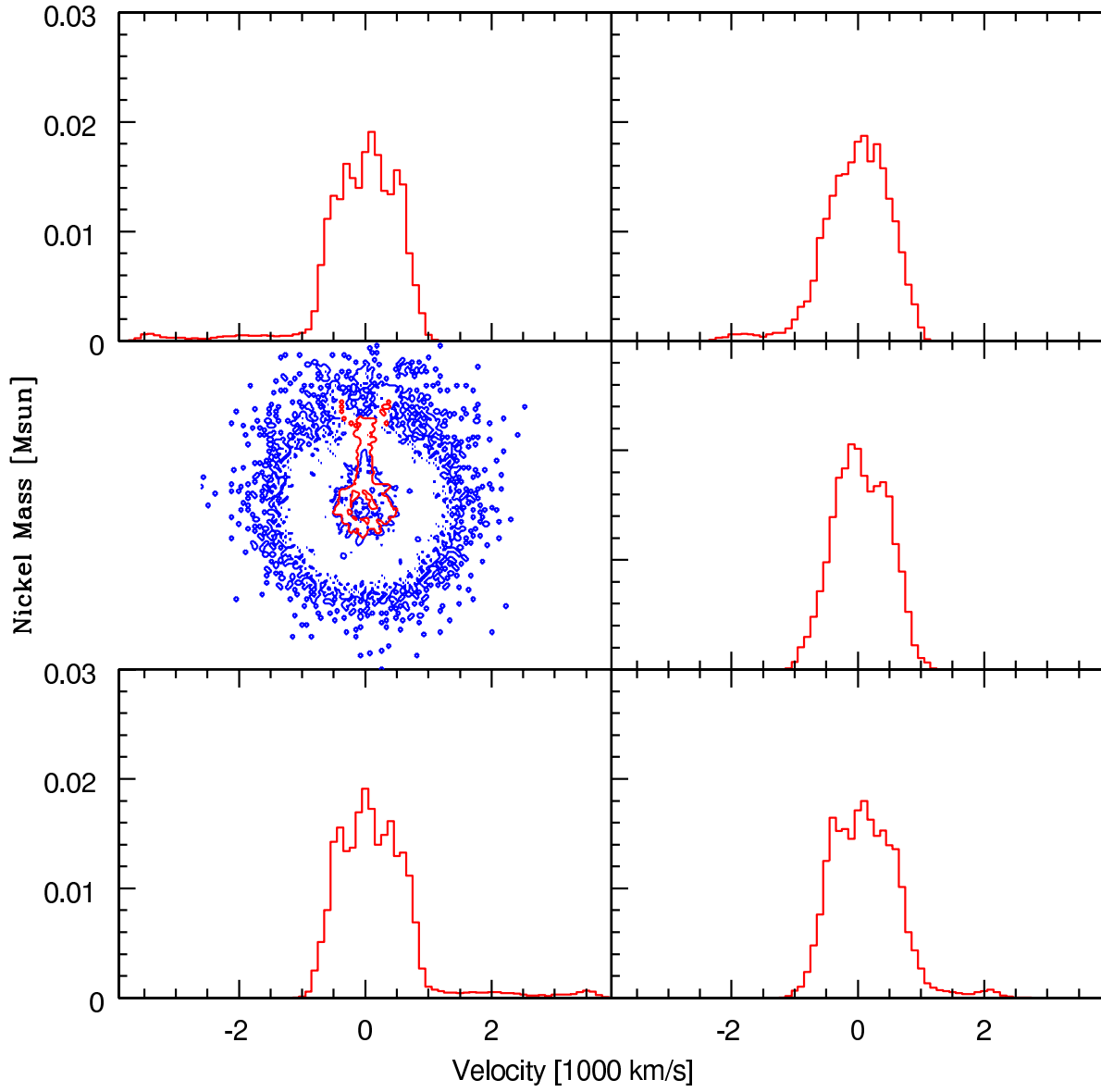


Fig. 9.— Same as previous figure, but for model f2th20.

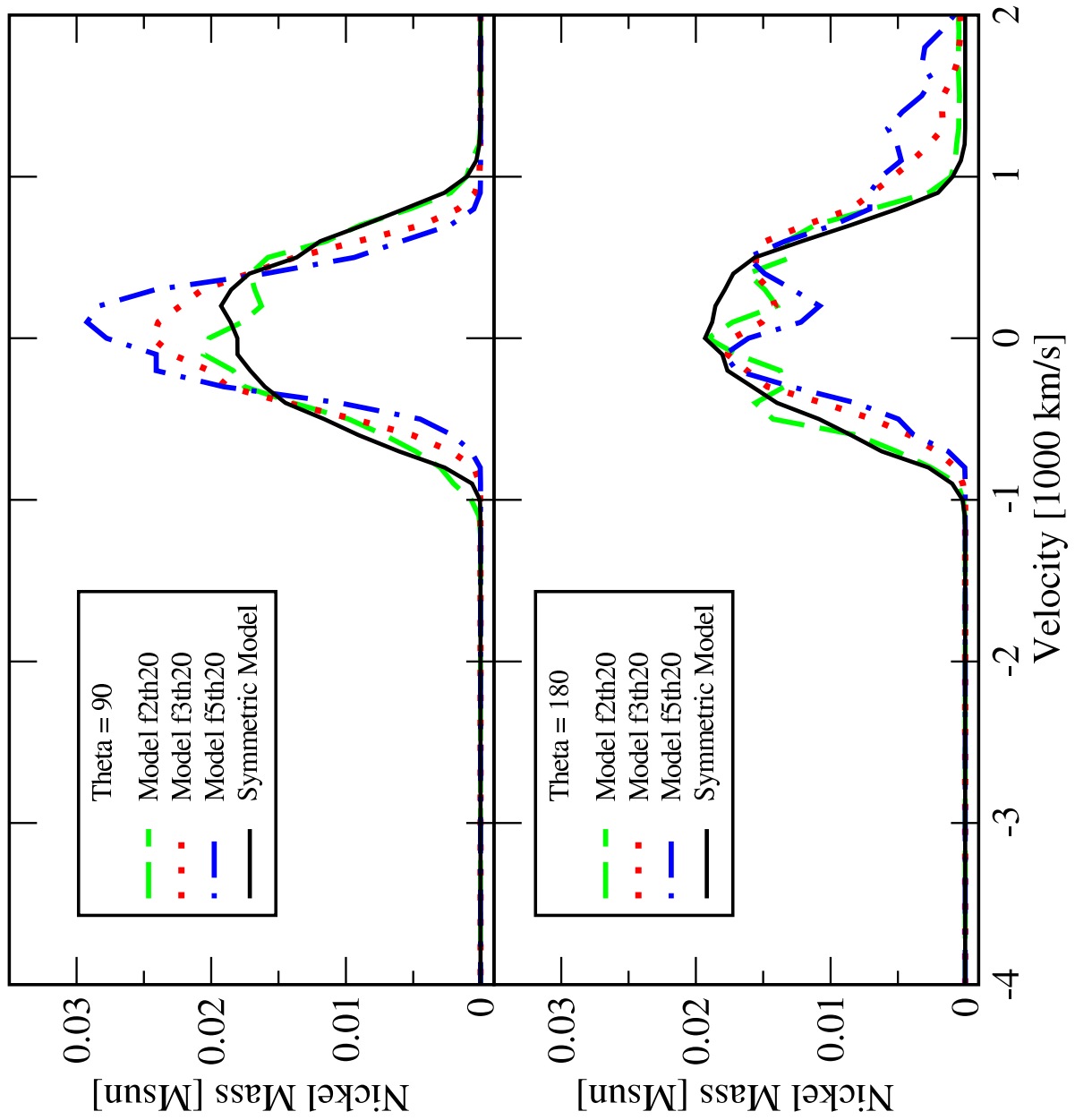


Fig. 10.— Underlying nickel distributions for the fXth20 models, with symmetric model distribution plotted for comparison.

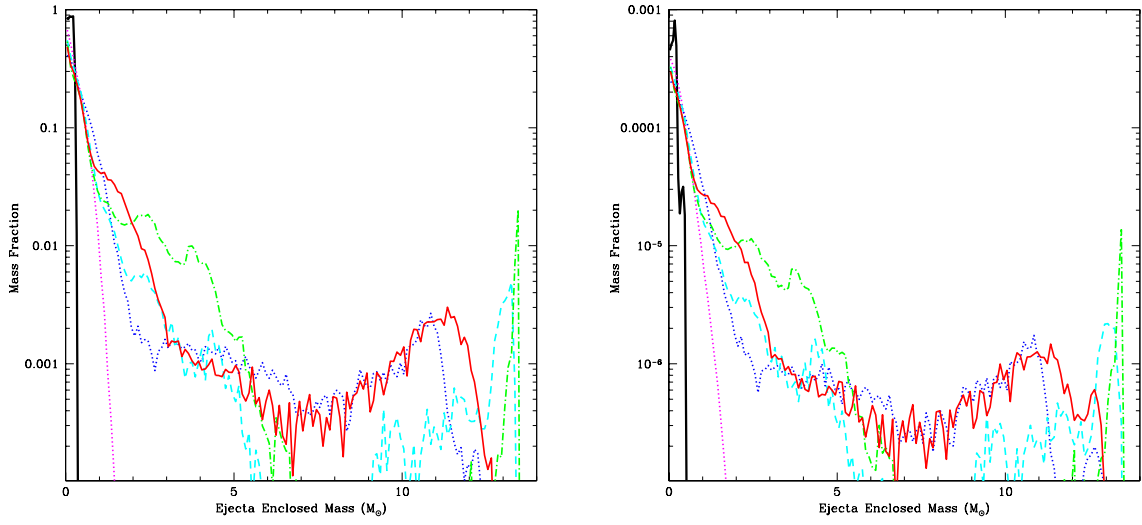


Fig. 11.— ^{56}Ni mass fraction (left) and ^{44}Ti mass fraction (bottom) plotted versus enclosed mass for our suite of explosion models. Dotted magenta line is model symm, dotted blue line is model f2th20, dashed cyan line is model f5th20, dash-dot green line is model f5th20, solid red is model f3th40 and the nearly vertical line is the initial condition (i.e. the result one would obtain had no mixing occurred).

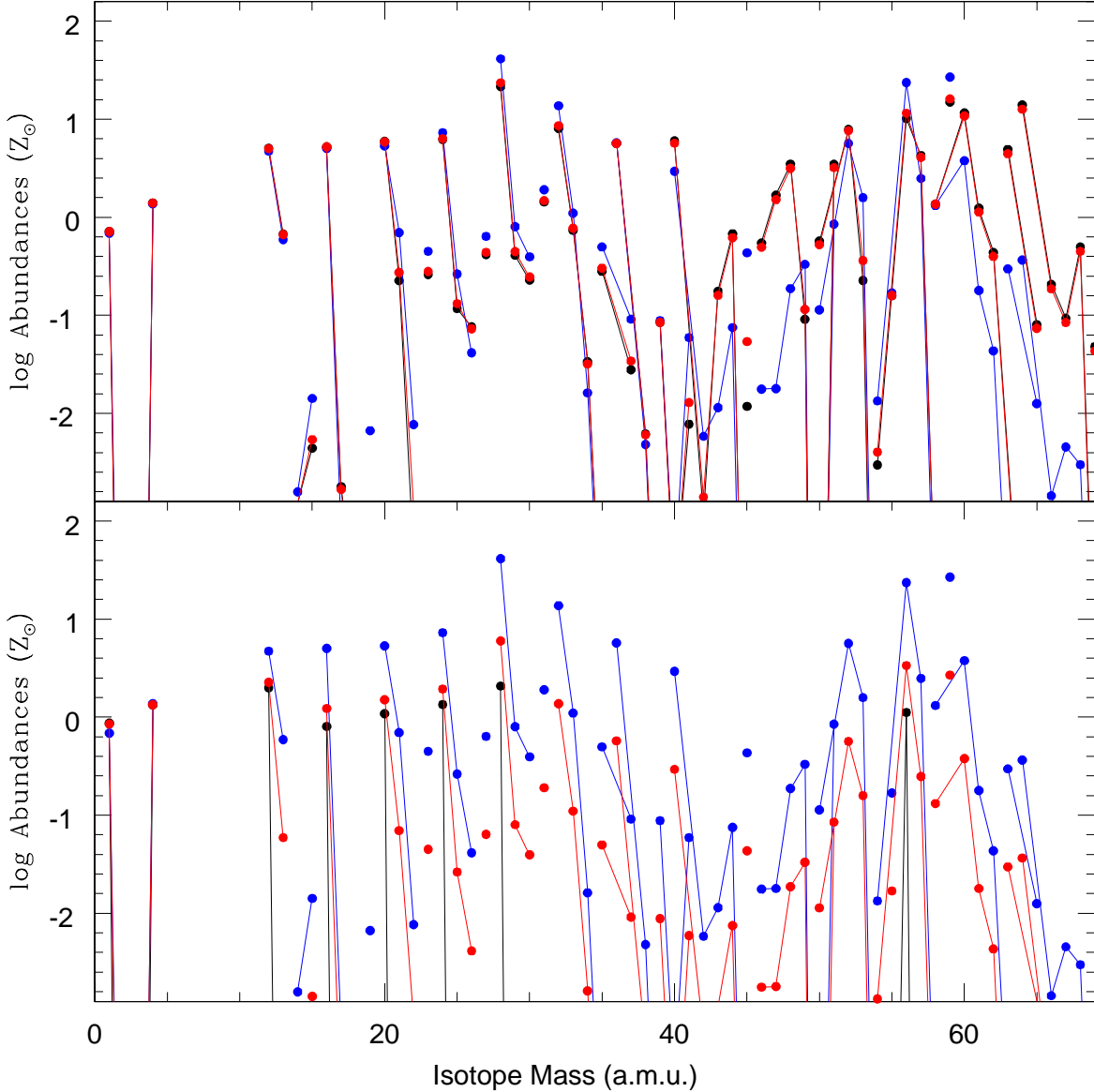


Fig. 12.— Top: Fractional abundance (in solar units) versus isotope mass for 1-dimensional models with $1.35, 6.5 \times 10^{51}$ ergs (black, blue respectively) and for a linear combination (90%,10% mix for the $1.35, 6.5 \times 10^{51}$ erg explosions) model. Note that the combined model which presents an extreme result for our current models is not too different from a 1.35×10^{51} erg explosion alone. Bottom: same set of abundances, but substituting a 0.1×10^{51} erg explosion for the 1.35×10^{51} erg explosion. Although such a result does not correspond to our current simulations, it is an example of where asymmetric explosions may drastically alter our expectations of the nuclear yields. This example corresponds to an explosion which ultimately produces a black hole, though the yields are not too different than a normal supernova explosion. However, be aware that these results are very rough estimates, based on very simplistic calculations.

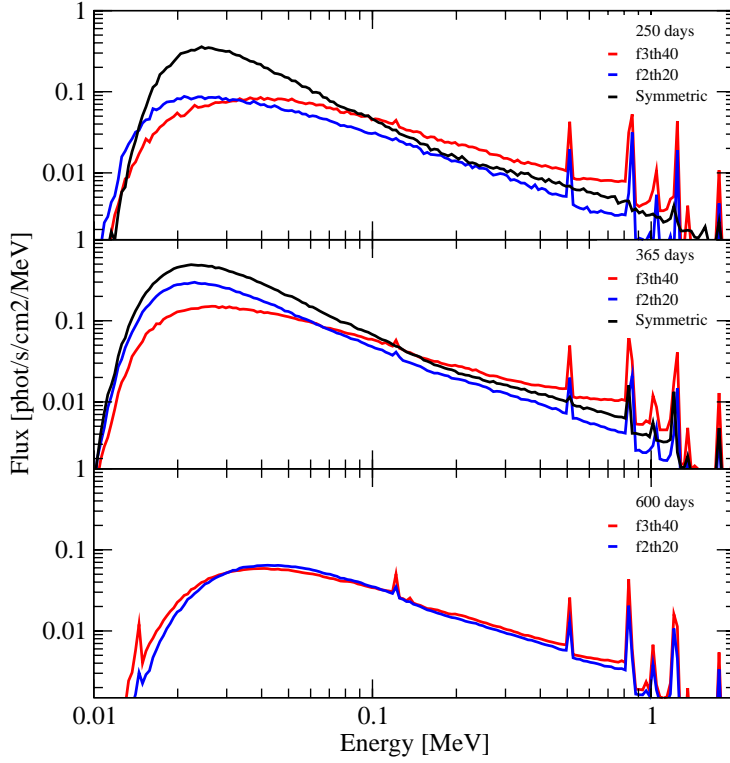


Fig. 13.— Logarithmic plot of total hard X- and γ -ray spectrum at $t = 365$ d for models f3th40 (red line), f2th20 (blue line) and Symmetric (black line) for 3 different times ($t = 250$ d, 365 d and 600 d.) The flux was calculated assuming a distance of 60 kpc. The f3th40 model evolves more slowly in time, and the Symmetric model has a brighter low energy continuum at all epochs.

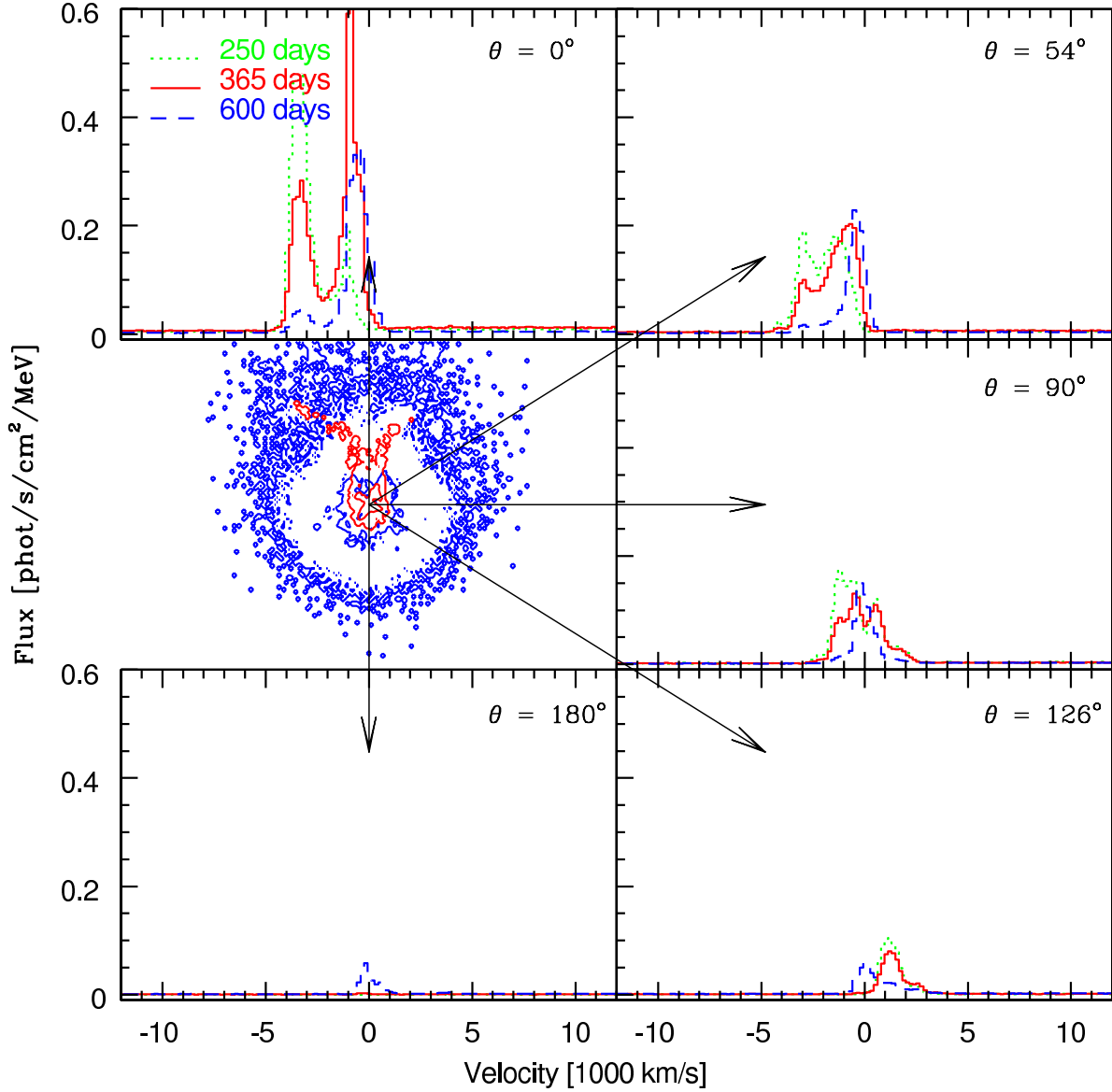


Fig. 14.— Line profiles of the ^{56}Co 847 keV decay line for model f3th40 at $t = 365$ days. Central panel on the left shows a contour plot of density (blue) and cobalt number density (red). Surrounding panels represent line profiles for the set of viewing angles depicted by the black vectors overplotted on the density contours. The emission in the line profiles arises predominantly from the cobalt ejected along the enhanced explosion lobe. Due to the homologous nature of the ejecta, the structure in the lines can be understood by summing this extended cobalt material along lines perpendicular to the viewing angle vectors. See text for a more in depth discussion.

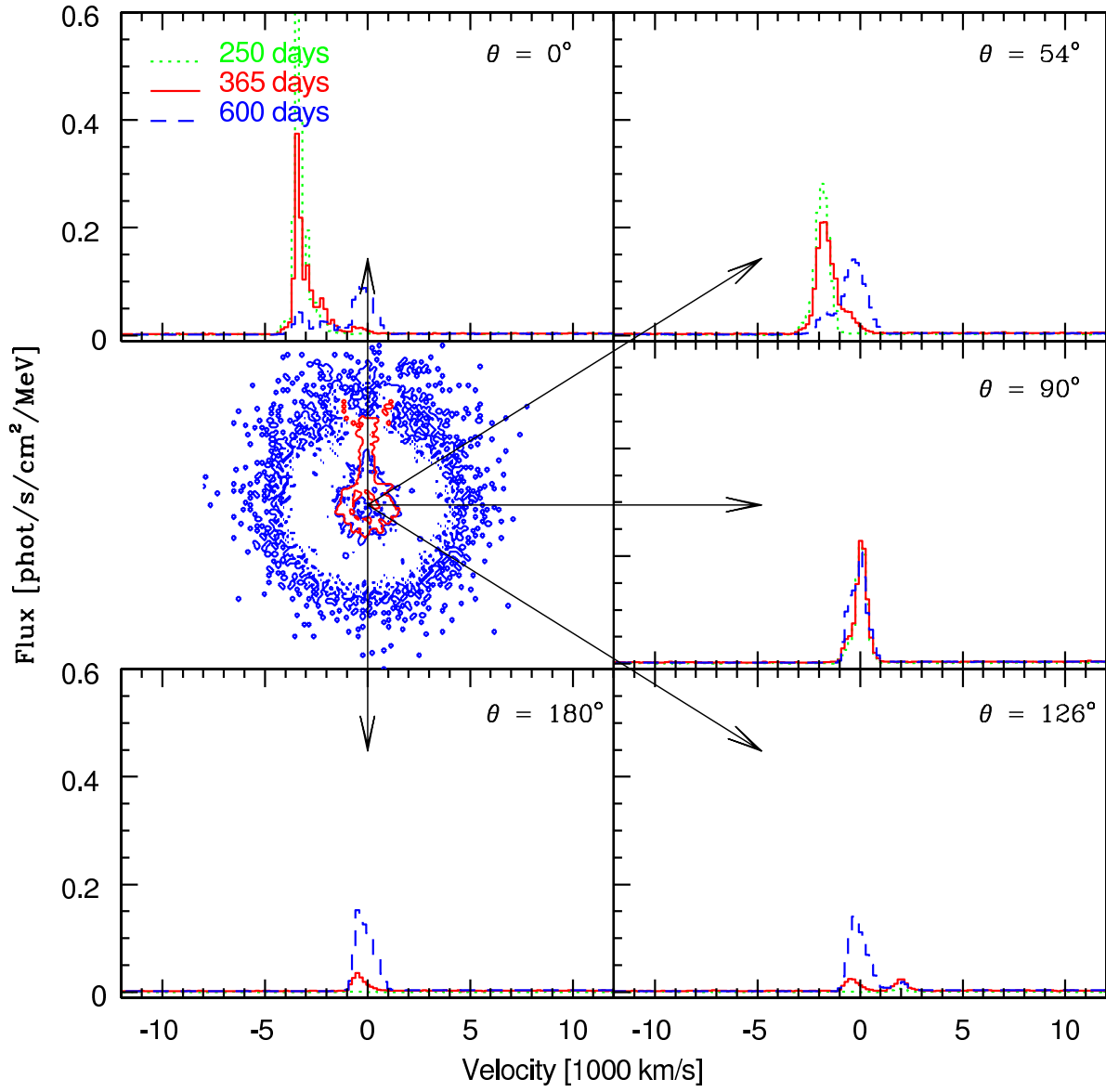


Fig. 15.— Same as previous figure, but for model f2th20.

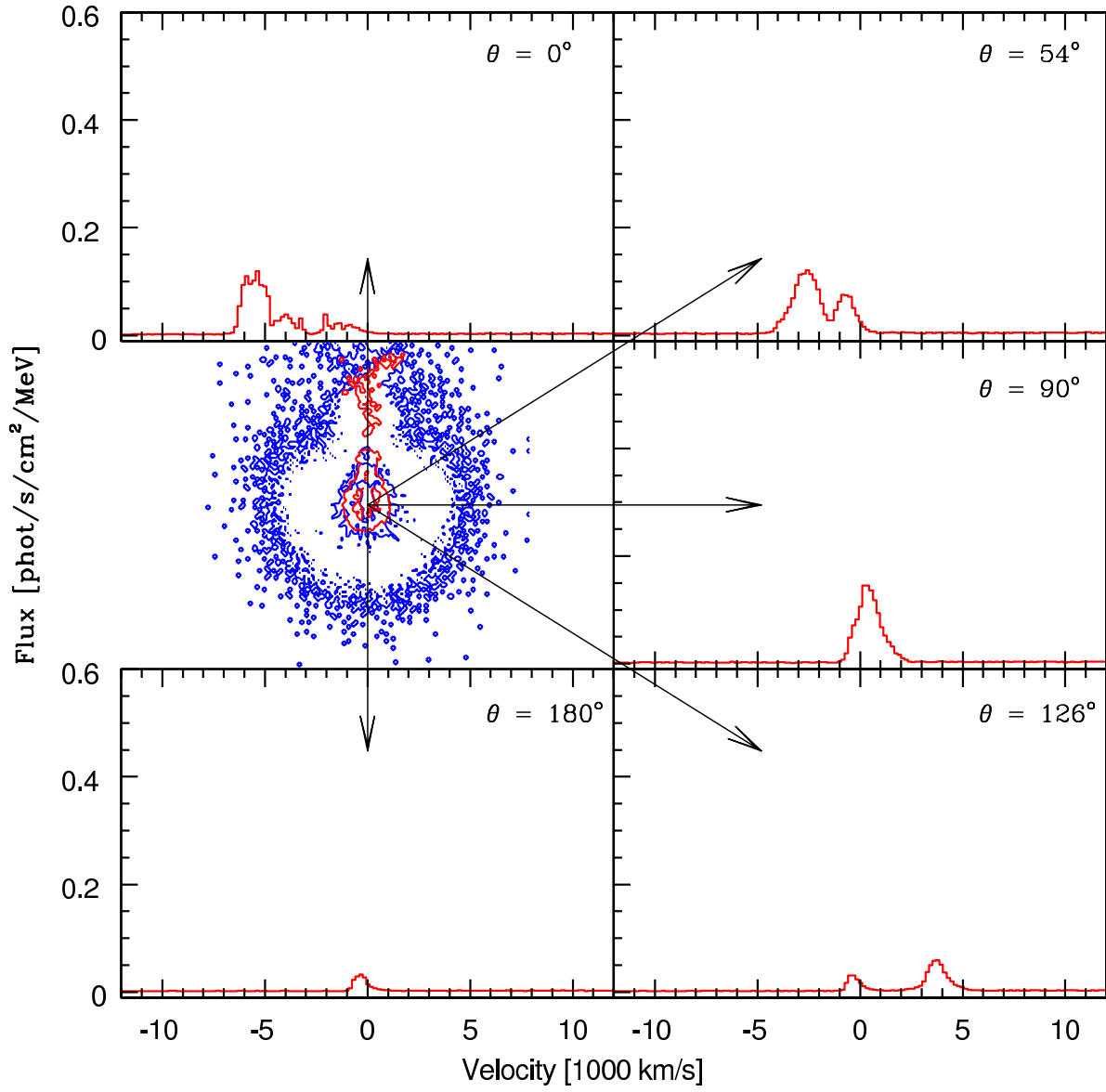


Fig. 16.— Same as previous figure, but for model f3th20.

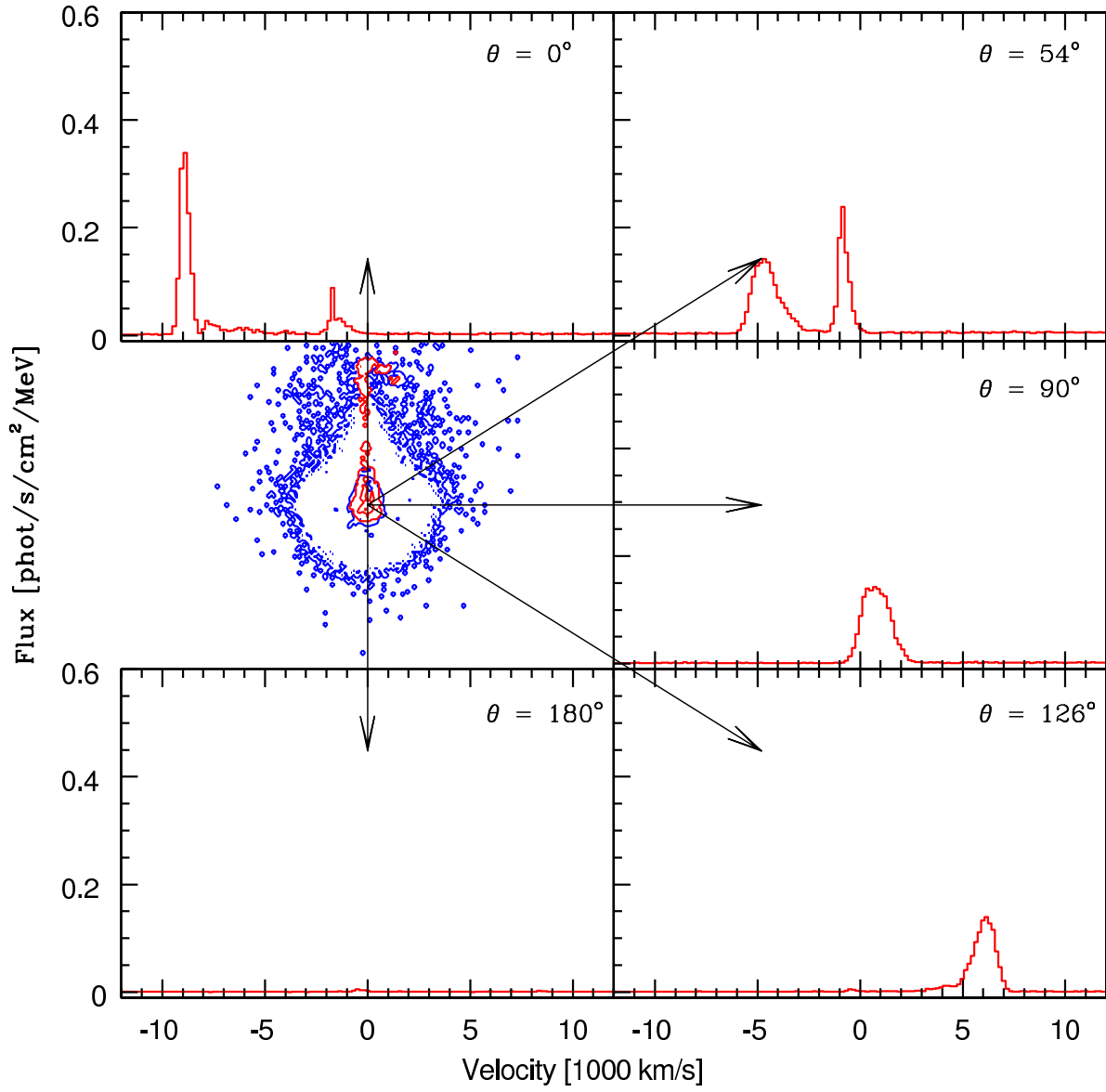


Fig. 17.— Same as previous figure, but for model f5th20.

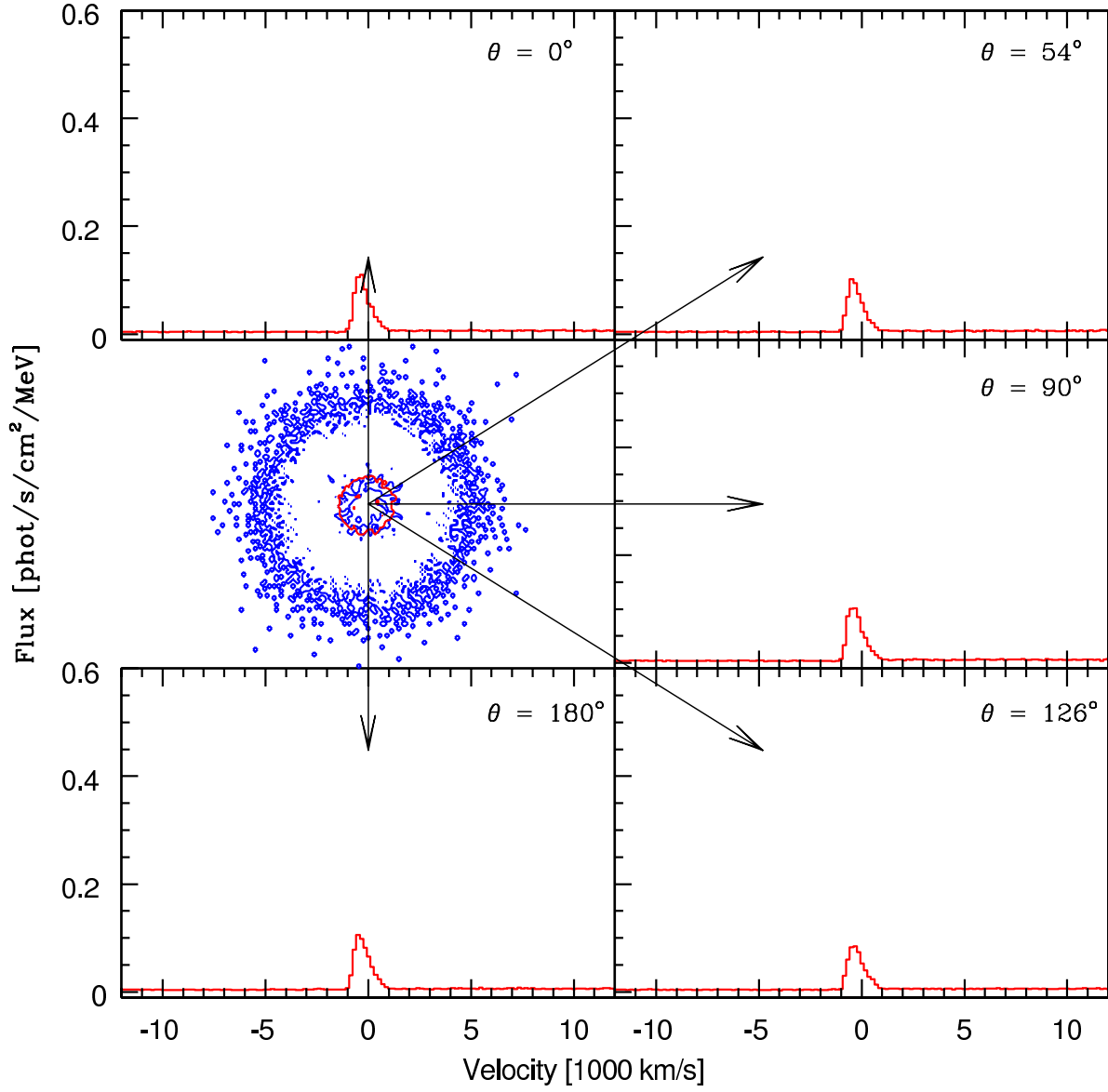


Fig. 18.— Same as previous figure, but for model symm.